Impact of milling conditions on hard and soft carbon properties and performance in potassium-ion batteries

Louiza LARBI[a,b], Badre LARHRIB[c], Lénaïc MADEC[c,d], Cyril VAULOT[a,b], Laure MONCONDUIT[d,e,*], Camelia MATEI GHIMBEU[a,b,d,*]

[a] *Université de Haute-Alsace, Institut de Science des Matériaux de Mulhouse (IS2M), CNRS UMR 7361, F-68100 Mulhouse, France.*

[b] *Université de Strasbourg, F-67081 Strasbourg, France.*

[c] *Universite de Pau et des Pays de l'Adour, E2S UPPA, CNRS, IPREM, Pau, France*

[d] *Réseau sur le Stockage Electrochimique de l'Energie, CNRS FR3459, Amiens, France.*

[e] *ICGM, Univ. Montpellier, CNRS, ENSCM, Montpellier, France.*

Corresponding author:

*E-mail: camelia.ghimbeu@uha.fr; laure.monconduit@umontpellier.fr.

Graphical Abstract

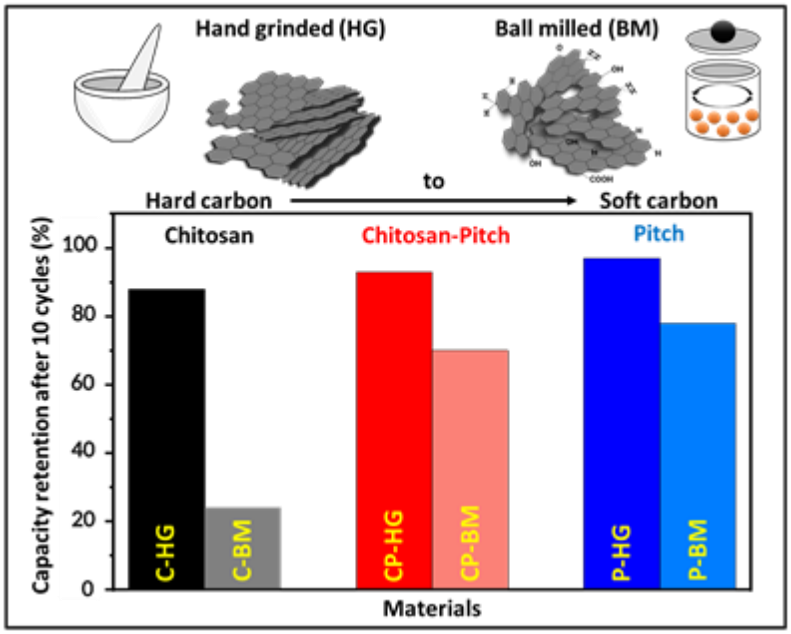

Abstract

Hard carbon (HC) and soft carbon (SC) are very attractive electrode materials for K-ion batteries (KIBs). However, specific attention must be devoted to electrode preparation to preserve their properties. This work reports the effects of milling conditions (ball milling and hand grinding) used for HC and SC (or mixtures) on their properties and electrochemical performance. The properties were strongly affected by the use of ball milling instead of hand grinding. Ball milling gave a homogeneous morphology with small particles, but a more disorganized structure containing impurities. A higher specific surface area, more oxygen-containing groups and a greater active surface area were also generated. In addition, the more disorganized materials with more oxygen content (i.e., hard carbons) were most influenced by ball milling. These modified properties had a negative impact on the performance. In contrast, hand grinding of the latter materials provided the best initial coulombic efficiency (ICE) and greater capacity retention during cycling, i.e., 79% (HC) and 91% (SC) after 50 cycles. Postmortem XPS studies revealed the nature of the solid electrolyte interphase (SEI) and a possible reason for the low ICE. The SC was tested in a full cell vs. C-coated $KVPO_4F_{0.5}O_{0.5}$ and delivered promising performance at high C-rates.

Keywords

Hard carbon, soft carbon, ball milling, grinding, negative electrode, potassium-ion batteries.

1. Introduction

Potassium-ion batteries (KIBs) are alternatives to lithium-ion batteries (LIBs) and are currently under development to satisfy future demand. This is motivated by the potassium availability , promising performance and low cost expected technology[1]. The electrode material chemistry plays a crucial role in increasing the KIBs performance, and research is now focused on the design of new negative electrode materials and modification of the existing ones. Various materials have been proposed as negative electrode materials for KIBs; among them, carbon materials, *e.g.*, graphite, doped carbons, hard and soft carbons (HC and SC) and their composites, attracted much attention due to their availabilities, low costs, stabilities, and promising performance[2]. HC comprises a mixture of disordered and pseudo graphitic domains with open and closed pores that cannot be graphitized even at very high pyrolysis temperatures. In contrast, SC is a partially graphitized carbon with a tuneable and adjustable graphitization degree[2].

HC can be obtained from a wide variety of precursors, such as biomass and biopolymers, i.e., fruits and vegetable waste, phenolic resin, cellulose, and chitosan, while organic aromatic compounds such as pyrolytic petroleum coke and coal tar pitch are used for SC preparation[2–4]. Chitosan is an inexpensive, abundant, biodegradable, and nontoxic HC precursor that is used to prepare the negative electrodes for sodium-ion batteries (NIBs)[5]. On the other hand, pyrolysed pitch has used in negative electrodes for various battery systems [4,6,7]. Recently, it has also been proposed to prepare HC and SC mixed compounds as an attempt to combine the disordered-like structure of HC and the graphitised structure of SC to obtain an intermediary structure combining the long cycling life of HC with the high rate capability of SC[8].

Carbon materials are usually obtained as grainy powders depending on their precursors[9,10] and need to be ball milled before preparing the electrodes. This step is commonly used in industry as well. However, only a few papers reported and discussed the conditions used for

ball milling carbon powder and their effects on both the physico-chemical properties and electrochemical performance. Furthermore, these studies were focused only on LIBs and NIBs[9–11]. Ilic et al.[11] reported the impact of ball milling on both the porosity and the electrochemical performance of a commercially available HC material used for NIBs. The material was milled with two zirconia balls in a zirconia jar at 500 rpm for different time periods (5, 60 and 300 min) under air. The authors observed that the specific surface area (SSA), open porosity, and oxygen content increased with increasing milling time, while the carbon content decreased. When the materials were tested as negative electrodes in a half-cell vs. sodium metal, the irreversible capacities were increased by increased ball milling time. Monoclinic and tetragonal zirconia impurities from the jar and balls were also noticed, and their amounts increased with milling time. Bonino et al.[10] reported the impact of different milling times (10, 20, 45, and 90 min) on the properties of disordered carbon (derived from hexaphenyl benzene (HPB)) and their performance in LIBs. The material was ball milled in an air atmosphere using an agate cup, three agate balls, and a rotation rate of 580 rpm. It was found that the graphene interplanar distance (d_{002}), and the crystallite width (L_a) decreased with increasing milling time, while the crystallite heights (L_c) increased. The SSA also increased for milling times up to 45 min and then decreased for samples ball milled for 90 min. The performance of the materials tested in a half-cell vs. lithium metal showed that high milling times had a negative effect on the specific capacity during cycling and degraded the insertion/extraction capabilities due to the smaller spaces between the graphene layers. In another study, Yue et al.[12] studied the impact of the milling conditions on a highly graphitized expanded graphite (EG). Ball milling was carried out in air with stainless steel balls, ethanol as the milling medium, and a speed of 450 rpm for milling times of 60, 80 and 100 hours. An expansion of $d_{002,}$ was observed due to destruction of the structure and the creation of defects. These results were not consistent with results reported by Bonino et al.[10], probably due to the differences in the materials and the milling

conditions. In addition, the slurry mixing procedure and conditions are generally not mentioned in the scientific literature[6,13–16], although different methods can be used; these include magnetic stirring, mixers (Ultraturrax) and ball milling, and they can have an impact on the electrochemical performance[17]. It is worth mentioning that the latter method is the one most commonly used on the laboratory scale. Ponrouch et al.[17] investigated the impacts of three slurry preparation techniques (magnetic stirring, magnetic stirring with sonication and ball milling) on the electrochemical performance of mesoporous carbon microbeads in LIBs. The scanning electron microscopy (SEM) images of the electrodes showed that the mixing procedure had a substantial effect on the morphology of the pristine material and on the homogeneity of the resulting electrode. Furthermore, it was proven that soft milling conditions had enhanced the electrochemical performance, as indicated by the initial coulombic efficiency (ICE), the first charge capacity, and the capacity retention rate during cycling. Based on these studies, it is clear that the grinding conditions impact the properties of both the carbon and electrode, resulting in performance alteration. Therefore, careful consideration and optimization of the ball milling process are necessary to minimize the negative effects and maximize the electrochemical performance.

In this work, we report the effects of both soft hand grinding and ball milling on carbon materials with different graphitisation degrees (HC, SC and their mixture) on their physicochemical properties (morphologies, structures, textures, surface chemistries, and defects) and electrochemical performance in half-cells vs. potassium metal. It was found that ball milling lead to homogeneous morphology, but modifies the carbon chemistry and textural properties including a high irreversible capacity and poor cycling performance. Moreover, the materials were unequally affected, by these modifications. However, hand grinding preserved the physicochemical properties more effectively and afforded better electrochemical behaviour during testing as negative electrodes in half-cells and full KIBs.

2. Experimental

2.1 Material syntheses

HC, SC and a mixture (50 wt% : 50 wt%) were synthesized according to the synthesis procedure shown in Scheme 1):

I) The HC was prepared by direct pyrolysis of chitosan precursor. The choice of this biopolymer was motivated by its availability (extraction from shrimp-shell), its high carbon yield after pyrolysis and good performance of resulting HC in NIBs [5]. Briefly, the chitosan (low molecular weight, Mw = 159.00 g mol^{-1}, from Sigma Aldrich) was heat treated at 1500 °C (5 °C min^{-1} heating rate for 1h) in an alumina tube furnace under an atmosphere of argon (Ar) (15 L/h) fallowed by cooling at room temperature.

II) The SC and the mixture of HC and SC were prepared from pitch and a chitosan/pitch mixture, respectively, with two continuous pyrolysis steps at 600 °C (2 °C min^{-1} for 30 min) and then at 1500 °C (5 °C min^{-1} for 1h) under an Ar atmosphere in an alumina tube furnace. The low-temperature heating step was implemented to limit the pitch-volume expansion during pyrolysis.

The choice of temperature (1500 °C) is based on our previous work in which the impact of pyrolysis temperature on carbon properties on performance was studied, but also considering the published works in the literature[18,19]. At this temperature (1500 °C), a good compromise between a large interlayer space to accommodate the K^+ size, a low specific surface area (SSA) and defects to limit irreversibility in the battery.

The obtained carbon materials were separated into two parts and used for hand grinding and ball milling. Half of material (~3-4 g) was hand ground (HG) to obtain C-HG, CP-HG, and P-HG (where **C** stands for chitosan, **CP** stands for the mixture of chitosan and pitch, and **P** stands for pitch). A quantity of about 3-4 g was placed in an agate mortar and manually grinded during

approximately~40 minutes. The remaining half quantity was ball milled (BM) with a ball miller (Retsch PM 100 planetary) in an 80 mL zirconia jar and with 5 zirconia balls (20 mm) at 200 rpm for 10 cycles (10 min/cycle with 10 min of rest between cycles). The resulting ball milled (BM) samples were denoted as C-BM, CP-BM and P-BM.

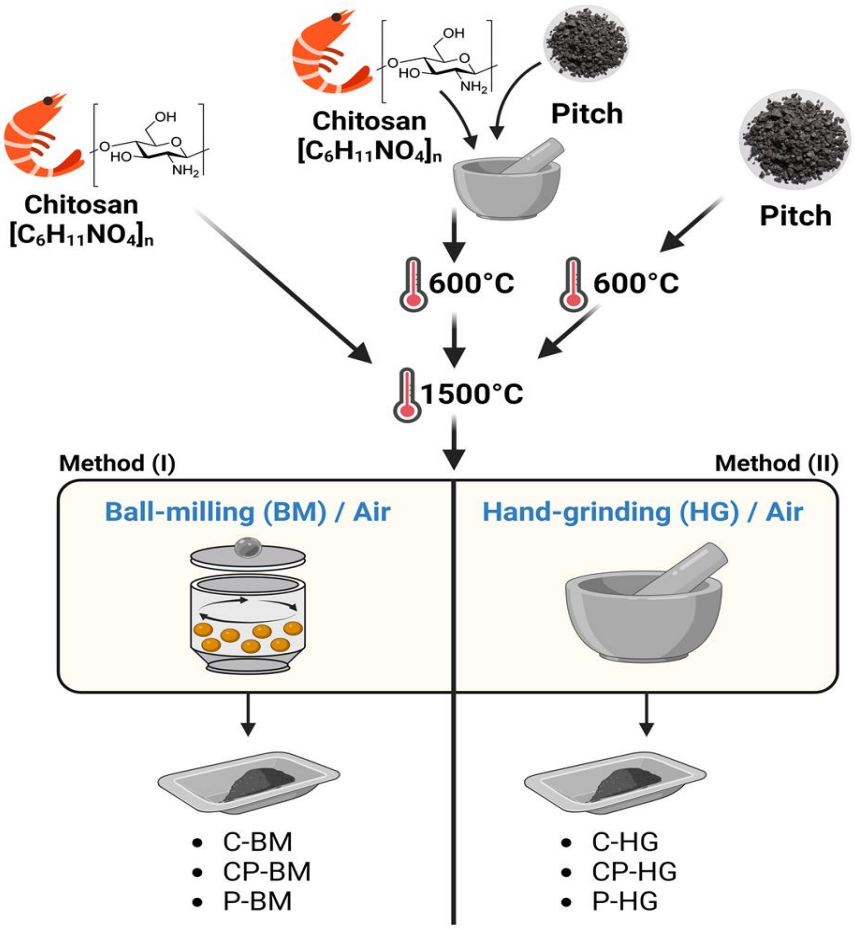

Scheme 1: Schematic representation of the synthetic process for the ball-milled and hand-ground materials (created by the authors with BioRender.com).

2.2 Material characterization

Thermogravimetric analyses (TGA) of the three precursors (C, CP and P) were performed with a Mettler Toledo instrument to determine their carbon yields. Each sample was heated from 30 to 900 °C at a heating rate of 5 °C min^{-1} in an alumina (Al_2O_3) crucible under a N_2 atmosphere.

The morphologies of the BM and HG materials were determined with scanning electron microscopy (SEM) with an FEI Quanta 400 scanning electron microscope. The particle sizes were estimated with ImageJ software and different SEM images. X-ray diffraction (XRD) patterns were obtained with a Bruker D8 Advance diffractometer with flat-plate Bragg–Brentano *θ-θ* geometry. An angular range of 10-90° with a step size of 0.01° (2θ scale) and a copper wavelength of 1.5406 Å were used for data acquisition. The spacing between the graphene planes, d_{002}, was calculated from the graphite diffraction peak (002) with the Bragg Equation (1):[20,21]

$$d_{(002)} = \frac{\lambda}{2sin\,\theta} \qquad (1)$$

where λ is the X-ray wavelength (1.5406 Å) and θ is the scattering angle corresponding to the peak position.

The heights (L_c) and widths (L_a) of the stacked graphene layers were calculated from the full width at half maximum (FWHM) of the (002) and (101) diffraction peaks, respectively, based on the Scherrer formula. (2):[20,21].

$$L = \frac{K\lambda}{Bcos\theta} \qquad (2)$$

where K is a sharp factor and has values of 0.91 for L_c and 1.84 for L_a, and B is the full width at half maximum of the peak (in radians). It is worth to mention that regarding the FWHM, The (100) and (101) reflections are effectively separated by around 2.2°2q (Cu Ka1), which in these materials, often poorly organized or with very small coherent diffraction domains, inevitably implies a significant overlap between these two reflections. It will therefore be difficult to assess the real contribution of one to the other in such cases, whatever the method chosen for estimating the FWHM. However, the intensity ratio of the two lines I(101)/I(100) obtained on

the basis of the crystal structure of graphite (COD 9011577), i.e. around 175/35, ie: 5 to 1, we considered that the extracted FWHM would be essentially attributed to the (101) line. Of course, the raw value obtained has no real individual meaning. However, by retaining this methodology for discussion for an identical family of materials, it remains possible to extract trends. The local structure was examined by high-resolution microscopy (HRTEM) with a JEOL instrument (ARM-200F model) operated at 200 kV. Textural characteristics such as the specific surface area, pore volume and pore size distribution were evaluated with a Micrometrics ASAP 2420 instrument using N_2 adsorption (77 K). The materials were outgazed under vacuum for 12 hours at 300 °C to remove physiosorbed molecules. The Brunauer - Emmett – Teller (BET) specific SSA was determined from the linear plot in the relative pressure range of 0.05 – 0.3 P/P_0 for N_2. The pore volume was calculated on the N_2 at P/P0 of 0.99 on the N_2 adsorption branch. The material pore size distribution (PSD) from the N_2 isotherms was determined by SAIEUS 2.02 software (Micrometrics) using the two-dimension non-local density functional theory (2D-NLDFT) for carbon materials and the heterogeneous surface model. The densities of the materials were measured with an Accupyc 1330 pycnometer from Micromeritics; helium gas was added after the samples were outgassed at 300 °C for 12 hours under vacuum. The closed and open pore ratios (R_{OP} and R_{CP}) were calculated from the total pore volume measured by N_2 sorption at 0.99 P/P_0, the helium density and Equations (4) and (5) [5,22].

Thermal programmed desorption coupled with mass spectrometry (TPD-MS) was used to gain insight into the natures and amounts of oxygen-containing functional groups in the bulk materials. Furthermore, the same technique enabled quantification of the active surface area (ASA). The TPD-MS analyses were performed with a laboratory-built (IS2M) system described elsewhere [23,24,25].

2.3 Electrochemical Characterization

2.3.1 Electrode preparation

Electrodes from the BM materials (C-BM, CP-BM and P-BM) were prepared from the active material, 90 wt %, poly(vinylidene fluoride, PVDF 5130 from Solvay, 5 wt.%) as a binder, and carbon black (Super C65 from Imerys, 5 wt %) as a conductive additive, with a mass ratio of 90:5:5 in N-methyl-2-pyrrolidone (NMP (purity ≥99) from Sigma–Aldrich); these components were mixed with a ball miller (PULVERISETTE 7) at 500 rpm for 1 hour. On the other hand, the hand ground electrodes (C-HG, CP-HG and P-HG) were prepared with the same protocols but with soft slurry preparation conditions. First, the PVDF binder was mixed with the NMP solvent at 200 rpm for 4 cycles of 5 minutes with a 10 min rest between cycles. Then, the active material and carbon black were added to the mixture and mixed for 6 more cycles of 10 minutes with 10 min of rest between cycles. The slurry was uniformly coated (150 µm thickness) onto an aluminium current collector (15 µm thick) with the doctor blade method (automatic film applicator). The electrodes (diameters of 9.5 cm and loadings of 1.6–2.2 mg cm^{-2}) were cut into round pieces with a specific disk cutter and then dried under dynamic vacuum at 80 °C for 24 h in a Büchi oven before they were introduced into an argon-filled glove box (MBRAUN) (O_2<0.5 ppm, H_2O<0.5 ppm), where the coin cells were assembled.

2.3.2 Battery testing conditions

Electrochemical tests were performed with 2032-type coin cells in a controlled temperature room (~25 °C) with a VMP 3 multichannel system (BioLogic, France) by assembling two cells of each material to ensure the reproducibility of the results. The coin cells were assembled with the HG and BM materials, glass microfiber filter (Whatman, Grade GF/D) separators, potassium metal as a reference and as a counter electrode (i.e., half-cell configuration) and 0.8 M KPF_6 in ethylene carbonate and diethyl carbonate (EC/DEC, 50: 50 v/v) as the electrolyte.

It is worth mentioning that K metal electrodes were prepared from K ingots (Alfa Aesar, 99.95%) according to the procedure described in our previous paper[25]. Galvanostatic charge/discharge tests were performed between 2.0 and 0.01 V (vs. K^+/K) in half-cells at C/10 (C=23 mA g^{-1}) for 50 cycles.

2.3.3 Postmortem X-ray photoelectron spectroscopy (XPS)

XPS characterization was performed with an Escalab 250 Xi spectrometer with monochromatized Al Kα radiation (hν = 1486.6 eV). P-HG electrodes, as obtained after 12 hours at the OCV and after the 1st and 5th depotassiation steps. They were extracted from the cell, washed two times for 1 min with 2 mL of DEC and dried for 5 h. Next, they were transferred directly into the XPS system from a connected argon-filled glove box, which ensured there was no moisture/air exposure.

The analyses were performed with the standard charge compensation mode and an elliptic 325 × 650 μm X-ray beam spot. Core level spectra were recorded with a 20 eV constant pass energy with 0.15 eV step sizes and iterative scans with dwell times of 500 ms to observe any degradation. Peak calibration, analyses and attributions were based on previous studies.[26]

2.4 Full cell assembly

Full cells were assembled with P-HG as the negative electrode and $KVPO_4F_{0.5}O_{0.5}$/C (KVPFO/C) as the positive electrode as shown in Scheme 2. The latter was synthesized via a solid-state route and C-coated via the approach reported in our previous work[27–29]. The areal capacities of both the positive and negative electrodes corresponded to the practical capacities obtained experimentally with half-cells. Thus, in assembling the P-HG full coin-cells (CR2032 316 L were used), the previously optimized parameters were applied[30].

The optimal negative/positive electrode diameter ratio (11/9.5 in mm) was used in a 3-electrode Swagelok T cell (i.e., a full cell with K-metal reference). After an open circuit voltage (OCV) was applied for 12 h, 5 cycles were performed at C/10 with potential ranges of 2.0–4.8 V, 3.0–4.8 V and 0.01–2.0 V for $E_{KVPFO/C}$ (E_{WE}), $E_{KVPFO/C\text{-}P\text{-}HG}$ ($E_{WE\text{-}CE}$) and $E_{P\text{-}HG}$ (E_{CE}), respectively.

The negative/positive electrode capacity ratio (1.16 ± 0.02) was used for both the 3-electrode Swagelok T cells and full coin-cells. The load of the P-HG electrode was fixed to 2.1 $mg_{active\text{-}material}/cm^2$, while the load of the KVPFO/C electrode was 5 $mg_{active\text{-}material}/cm^2$, corresponding to a capacity ratio of 1.17. The capacity was calculated based on the KVPFO/C active material.

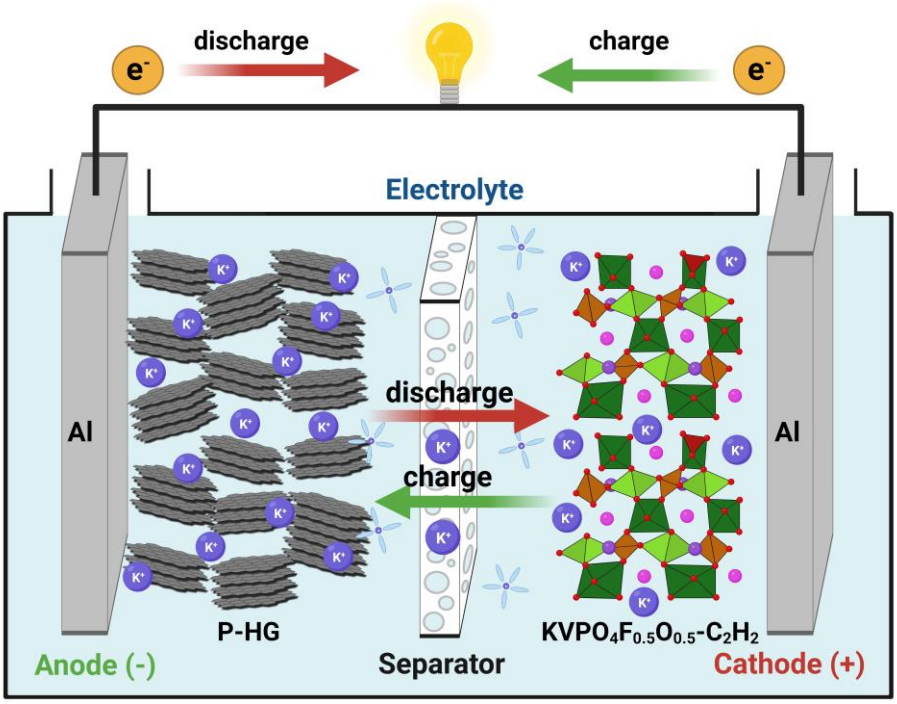

Scheme 2: Schematic representation of the realized full cell using SC as a negative electrode and $KVPO_4F_{0.5}O_{0.5}$-C_2H_2 as a positive electrode (created by the authors with BioRender.com).

3. Results and discussion

3.1 Morphology, Structure, Texture and Surface properties

The synthesized materials exhibited high carbon yields of 30, 36 and 45% for C, CP and P, respectively, as shown by the TGA results in Figure S1. For P, a significant amount of gas was released during pyrolysis, which led to volume expansion and a foam-like shape[31,32], as shown in Figure S2. This is rarely mentioned in the literature when reporting this carbon precursor[6,33], although this behaviour might limit the amount of material during the thermal treatment. Alternatively, a stabilization step at a lower temperature could be used before the pyrolysis step to avoid this phenomenon[31,32,34].

The morphologies of the HG and BM materials were examined by SEM, as shown in Figure 1 a-c and a'-c'. Large particles were contained in the HG materials (Figure 1a-c): ~40 µm for C-HG and ~55 µm for both CP-HG and P-HG. For the latter materials, the sizes and shapes of the particles were more heterogeneous. On the other hand, after ball milling (Figure 1a'-c'), significant reductions in the particle sizes led to average particle sizes of ~8–12 µm for all of the ball milled materials, furthermore, small white particles were noticed for the BM materials (Figure 1a'-c') which are probably ZrO_2 as showed by XRD and XPS results. The smallest particles were observed for C-BM, showing that it was more affected than the others. Generally, the HG materials exhibited heterogeneous morphologies, which was due to less control of hand grinding compared to ball milling.

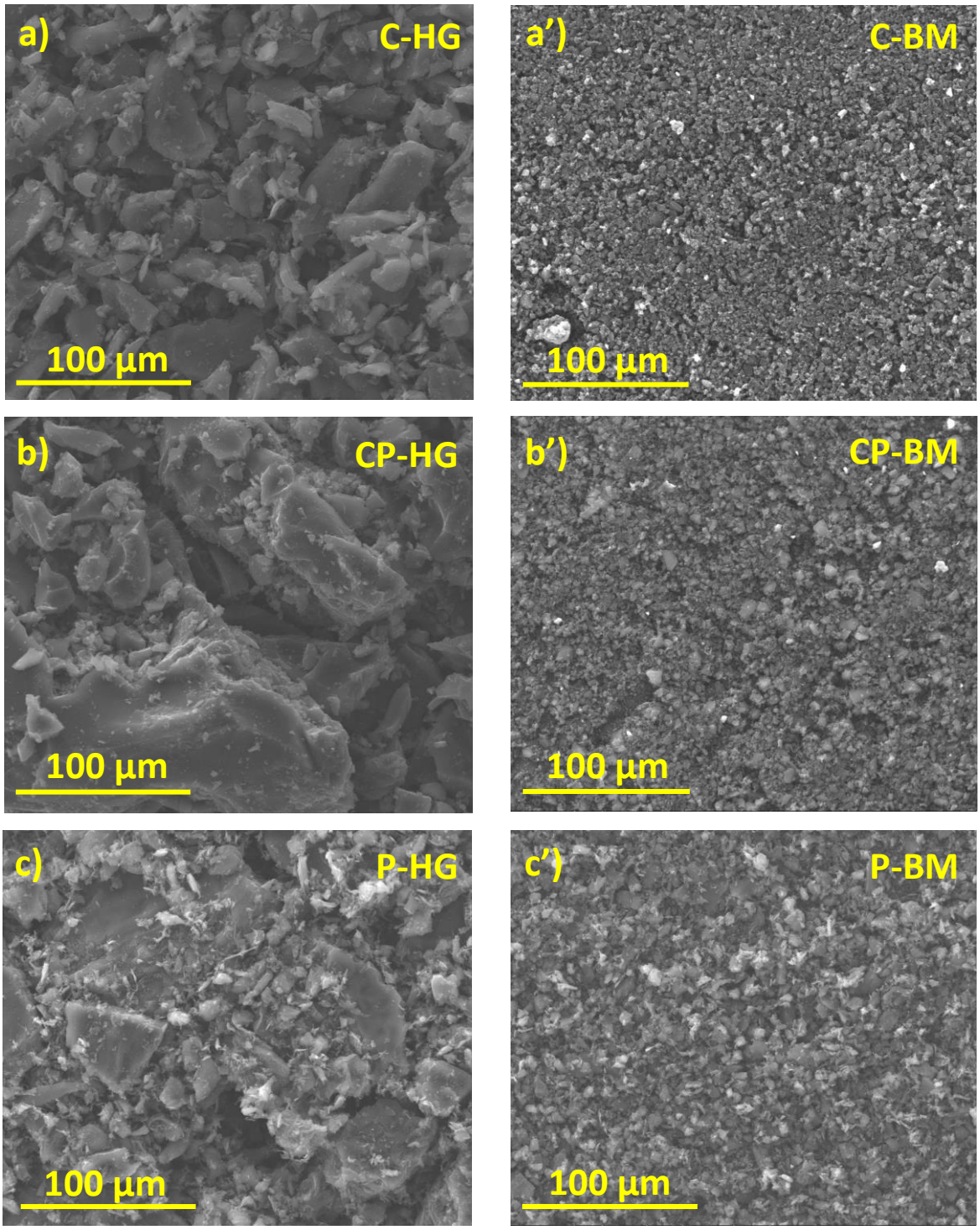

Figure 1: (left) SEM images of (a) C-HG, (b) CP-HG and (c) P-HG; (right) (a') SEM images of C-BM, (b') CP-BM and (c') P-BM.

The structures of the materials were analysed with HRTEM and XRD (Figure 2). A HRTEM image of C-HG (Figure 2a) showed a typical hard carbon structure that combined randomly orientated disordered graphene domains and pseudographitic domains[35], where few short graphene sheets were stacked in 3–5 layers. A more organized structure with more stacked carbon layers (~ 4–7) was observed for CP (Figure 2b). The increased degree of graphitization was due to the addition of pitch, which contains aromatic units that undergo graphitization. In fact, pure pitch-derived carbon, P-HG, exhibited the typical structure of soft carbon[34,36] (Figure 2c), with a highly organized structure, more abundant stacked carbon layers in different directions (>10 layers), and larger graphene sheets compared to both CP-HG and C-HG.

As illustrated in Figure 2d, the XRD patterns of the HG samples exhibited a first diffraction peak at $2\theta \approx 24\text{-}25°$, which was indexed to the (002) plane of graphite. The peak was more intense and narrower and shifted to higher 2θ angles (24.50°– 25.7°) for the materials containing pitch (CP-HG and P-HG), indicating an increase in the graphitization degree on going from C-HG to CP-HG to P-HG. This was confirmed by the interplanar distance, d_{002}, which decreased from 3.62 Å (C-HG) to 3.46 for both CP-HG and P-HG, respectively (Table 1 and Figure S3a). The three materials exhibited other peaks at $2\theta \approx 43°$ and $2\theta \approx 79°$, which were attributed to the (100) and (110) planes of graphite, respectively, with an additional peak for CP-HG and P-HG at $2\theta \approx 54°$, indexed to the (004) planes. On the other hand, the BM materials (Figure 2e) show slightly larger and less intense peaks than the HG materials, as confirmed by the full width at half maximum (FWHM) values, which increased (Table 1). In addition, a slight increase in d_{002} was only observed for hard carbon, from 3.64 Å (C-HG) to 3.62 Å (C-BM), while the CP-BM and P-BM maintained the same interplanar distances (Table 1 and Figure S3a). These variations (FWHM and d_{002}) were due to degradation of the material structures during BM, particularly for the more disorganized materials (C-BM).

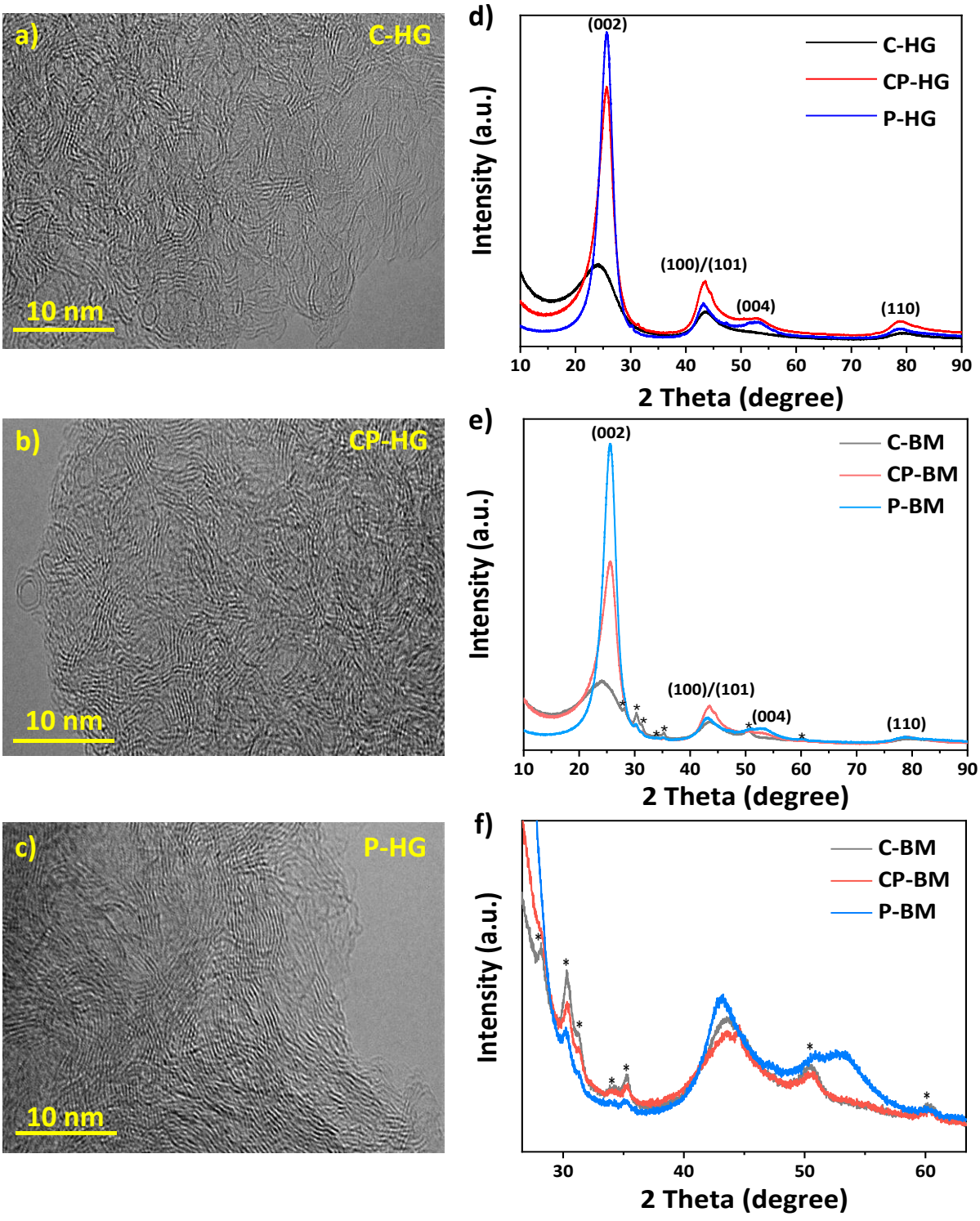

Figure 2: HRTEM images of (a) C-HG, (b) CP-HG and (c) P-HG; XRD data for the (d) hand ground and (e) ball milled materials (f), magnification of the 25-65° 2θ range, showing the ZrO_2 impurities of the ball milled materials. The "*" indicates ZrO_2, COD: 2300612 and 2108451.

In addition, impurities were detected in the BM materials (Figure 2e) with peaks at $2\theta \approx 28$, 30, 31, 35°, 50° and 60°; these corresponded to monoclinic and tetragonal zirconia (ZrO_2) (according to COD: 2108451 and 2300612), as shown by the enlarged image provided in Figure 2f. These impurities likely came from interactions of the carbon with the milling setup (jar and balls). The crystallite heights (L_c) along the *c* axis and the crystallite widths (L_a) along the *a* axis were calculated with the Scherrer formula from the (002) and (100) peaks, and the average number of stacked graphene layers was also estimated as L_c/d_{002} (Table 1).

L_a increased from C to CP to P for the HG materials, with values of 47, 58 and 59 Å, respectively (Table 1 and Figure S3b). The HG materials showed higher L_a values than the BM materials (43, 56, and 56 Å for C-BM, CP-BM and P-BM, respectively) as it can be seen in Table 1 and Figure S3b. L_c exhibited the same trend as L_a, with values that increased from 14 to 27 and 30 Å for the HG materials (C-HG, CP-HG and P-HG, respectively) and from 12 to 20 and 30 Å for the BM materials (C-BM, CP-BM and P-BM, respectively) as shown in Figure S3c. In addition, the calculated numbers of stacked graphene layers (L_c/d_{002}, Table 1**)** were 4, 8, and 9 for C-HG, CP-HG and P-HG, respectively (Table 1 and Figure S3d), which agrees with the HRTEM images (2–5, 2–8 and 7–15 layers, respectively). After BM, the L_c/d_{002} ratio was smaller than those of the HG materials (Table 1 and Figure S3d) and suggested degradation of the material structure due to ball milling. Different trends were reported in the literature for d_{002}, L_c and L_a due to heterogeneity of the samples prepared with ball milling, and the FWHM values were not discussed[10,12].

Table 1: Physico-chemical characteristics of the HG and BM materials: graphite interlayer distances (d_{002}), full widths at half maximum (FWHM), crystallite heights (L_c), crystallite widths (L_a), numbers of stacked graphene layers L_c/d_{002}, specific surface areas (SSA), total pore volumes (V_T), ratio open porosity (ROP), ratio closed porosity (RCP), active surface areas (ASA), proportions of oxygen-containing functional groups (CO_x) and He densities.

	Hand ground			**Ball milled**		
Materials	**C-HG**	**CP-HG**	**P-HG**	**C-BM**	**CP-BM**	**P-BM**
d_{002} (Å)	3.62	3.47	3.46	3.64	3.47	3.46
FWHM (°)	5.99	3.05	2.70	6.34	3.3	2.73
L_c (Å)	14	27	30	12	24	30
L_a (Å)	47	58	59	43	56	56
L_c/d_{002}	4	8	9	3	7	9
N_2 SSA ($m^2\ g^{-1}$)	3.5	2.3	2.7	115	29	28
V_T ($cm^3\ g^{-1}$)	0.006	0.004	0.006	0.104	0.049	0.041
ROP (%)	1.00	0.71	1.20	17.28	10.06	7.90
RCP (%)	26.45	22.25	9.36	11.04	9.38	7.50
ASA ($m^2\ g^{-1}$)	1.1	0.5	0.6	15	10	2
CO_X (mmol g^{-1})	0.07	0.08	0.07	0.98	0.420	0.290
He-density ($g\ cm^{-3}$)	1.71	1.80	2.11	2.01	2.08	2.13

The textural properties of the HG and BM materials were evaluated with N_2 sorption, and the HG materials (Figure 3a**)** all exhibited type II isotherms indicating nonporous materials. The BM materials (Figure 3b**)** showed two types of isotherms: the CP-BM and P-BM samples showed type II isotherms, and the C-BM sample showed a type I isotherm; the increased N_2 volume at low relative pressures, $P/P_0 < 0.1$, indicated the presence of micropores. In addition, the increased N_2 volume in the high relative pressure range, $P/P_0 > 0.8$, suggested intergrain porosity attributed to the formation of small particles after mechanical milling. Indeed, the SEM images showed smaller particle sizes for this material (Figure 1a').

The specific surface areas (SSAs) were determined and confirmed that all HG materials exhibited very small SSAs (<5 $m^2 g^{-1}$), even though BM increased them (Table 1). In particular, for hard carbon (C-BM), the N_2 SSA was 115 $m^2 g^{-1}$, which was 50 times higher than that of the hand ground counterpart, while for CP-BM and P-BM, the SSAs were 10 times higher than those of the hand ground materials.

These larger changes in the hard carbon textures arose from the disorganized structures and the higher oxygen contents, as shown by XPS measurements (Figure S4 and Table S1). High-energy BM led to degradation from the strong interactions with the balls and more organized structures for both the composite and soft carbon (CP-HG and P-HG). A high specific surface area was expected to have a negative influence on the electrochemical performance, especially the irreversible capacity; this was a consequence of electrolyte decomposition and excessive formation of the solid electrolyte interphase (SEI), which had a negative effect on the long-term cycling performance[37].

The pore size distribution (Figure S4a-b) showed three porosity ranges for all materials, including micropores with pore diameters < 2 nm, relatively few mesopores measuring ~3 nm; and finally, intergrain pores (~15–30 nm). It is worth noting that the BM materials displayed the same porosities but with higher pore volumes than the HG materials (Figure S4a-b and

Table 1). This increase in the pore volume especially for C-BM is due to the creation more porosity after ball milling, especially microporosity (pores < 2.0 nm), as revealed by the significant increase of the N_2 adsorbed volume in the pore size distribution (Figure S4b) The narrow pores on the C-BM sample might also lead to irreversible K^+ trapping[38].

This porosity can be due to the transformation of closed porosity to open porosity. As seen in Table 1, the closed porosity of the BM materials decreases while the open porosity increases, compared to the HG materials. Additionally, the formation of intergrain porosity is observed, as indicated by the increase in adsorbed N_2 at high P/P0 > 0.9 (Figure 3b and Figure S4ab). This behavior was explained in the literature for materials with small particle sizes (micrometers or nanometers) that form after the ball milling[39,40].

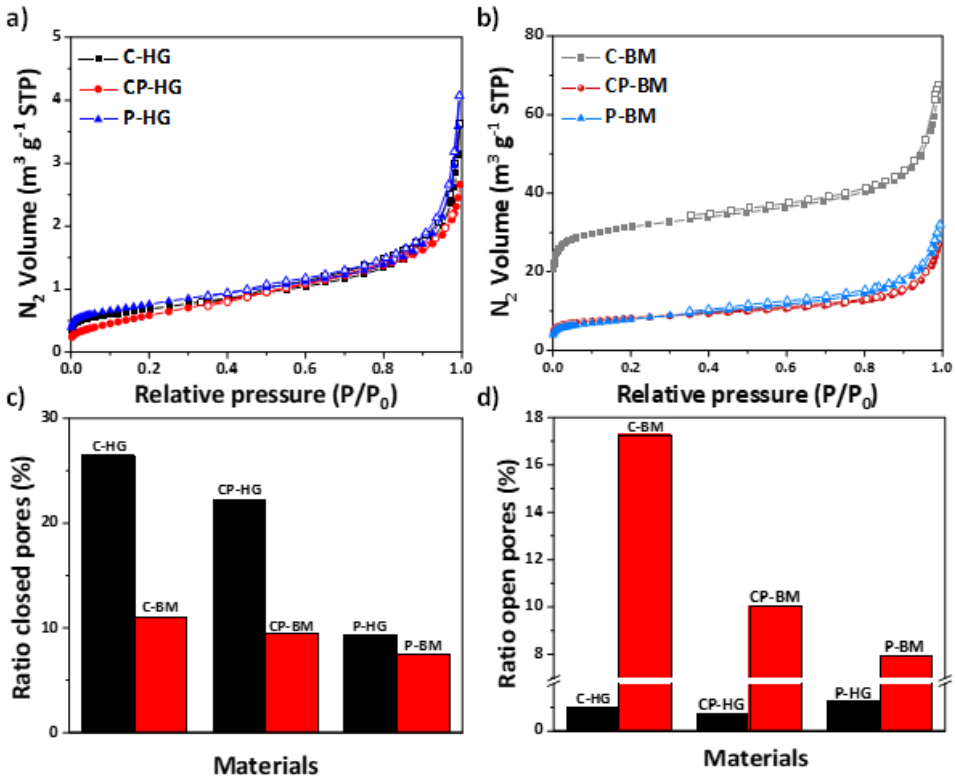

Figure 3: N_2 adsorption–desorption isotherms for the (a) hand ground and (b) ball milled materials; proportions of (c) closed and (d) open pores for the hand ground and ball milled materials.

The He-based densities of the HG and BM materials were measured (Figure S4c and Table 1), and the values increased with increasing structural organization for the HG (C-HG, CP-HG and P-HG) samples. On the other hand, the BM materials exhibited the same tendency with increasing He densities across the series however, the values were higher than those of the hand ground materials. The closed and open pore ratios of the HG and BM materials were calculated from the He densities and the total N_2 pore volumes (Table 1).

As shown in Table 1 and Figure 3c, the closed pore ratios of the HG materials were higher than those of the BM materials. This was caused by ball milling, which destroyed the closed pores in favour of the open pores (Figure 3d). Indeed, the BM materials showed considerable increases in open pores compared to the HG materials, with the highest impact for the C-BM (with a disorganized structure and a high N_2 SSA) followed by CP-BM and P-BM (more organized structures and low N_2 SSAs).

Figure S5a-c shows the XPS survey scans for C-HG, CP-HG, and P-HG, respectively. The hard carbon material (C-HG) contained more oxygen on the surface (O 1s), followed by CP-HG and P-HG materials (Table S1). On the other hand, the amount of C on the surface showed an opposite trend, with more for P-HG, followed by CP-HG and C-HG, as shown in Table S1. More carbon was expected to generate more insertion sites for larger amounts of K-ion storage, and fewer oxygen groups could limit electrolyte decomposition and cause SEI formation.

Some calcium impurities (2.68 at%) were observed for C-HG and arose from calcium carbonate ($CaCO_3$) contained in the precursor[5], which was extracted from crustacean shells (chitosan). Finally, small traces of other impurities were also detected (S, Na and Mo), which are thought to come from the furnace. Regarding the BM materials, the amounts of C were higher for the C-BM and CP-BM samples (91.50 at% and 94.14 at. %) compared to their HG counterparts (88.88 at% and 93.62 for C-HG and CP-HG), while the amount of O decreased from 8.44 at%

and 6.08 at% (C-HG and CP-HG) to 7.81 at% and 5.33 at% (C-BM and CP-BM, respectively). On the other hand, the amount of C in the P-BM decreased from 95.44 at% to 93.65 at%, while the amount of O increased from 4.18 at% to 5.59 at%. It was also seen that the calcium impurities in C-HG were not present in C-BM, probably due to reorganization of the material morphology. Other trace impurities were detected after BM, such as Zr (3d), from the zirconia jar and balls, and Si 2s and S 2p, probably from the mortar and/or Scotch tape used for XPS.

Because the surface chemistry assessed by XPS might be strongly affected by modification or reorganization of the particle sizes and surface, TPD-MS was used to probe the chemistries of the bulk materials. Figure 4a-d illustrates the TPD-MS profiles for the gases (CO_2, CO, H_2, and H_2O) desorbed during heating of the HG and BM samples under vacuum. The oxygen-containing functional groups generated CO_2 and CO, and the amounts were correlated with specific oxygen-containing functional groups based on their decomposition temperatures, as described in the literature[23,41].

CO_2 desorption (Figure 4a) began at ~100 °C for P-HG and CP-HG, indicating decomposition of the carboxylic acids at low temperature; however, the signal was very weak. In the case of C-HG, CO_2 decomposition occurred at higher temperatures, as shown by the intense and narrow peak at ~530 °C for the decomposition of $CaCO_3$ into CO_2 and CO[5]. Carbonates were present from the chitosan precursor. However, after ball milling, e.g., for (C-BM), this peak was less intense and hidden by a broad peak for CO_2 (100 to 700 °C). This suggested that the impurities were more dispersed in the materials and their sizes were probably reduced. This result consistent with the XPS data, with which Ca was not detected and therefore was no longer present on the surface. Furthermore, the large CO_2 profile suggested that ball milling formed other oxygen-containing groups, i.e., carboxyls, lactones (T < 400 °C) and anhydrides (T > 400 °C)[5,35,42,43].

On the other hand, CO decomposition (Figure 4b) began at ~ 300 °C for the HG and BM materials, indicating the decomposition of phenols, carbonyls, ethers and quinones. In addition, the BM materials exhibited more intense peaks than the HG materials, indicating more surface functional groups. Furthermore, H_2 desorption began at ~700 °C for the HG and BM materials **(**Figure 4c**)** and was attributed to cleavage of the C-H bonds in the BM materials, especially C-BM. This indicated greater structural disorganization and more defects in the BM materials. Water release began at ~100 °C (Figure 4d) due to physisorption into pores and/or secondary reactions between neighbouring oxygen functional groups (-COOH, -OH). Stronger peaks are observed for the BM chitosan-derived carbons (C-BM and CP-BM); therefore, these materials were more porous (higher specific surface areas) and/or more hydrophilic (more oxygen in their compositions). This water remained in the pores and blocked the passage of K ions, leading to parasitic reactions with the electrolyte. The TPD profiles (Figure 4a-d) indicated that the amounts of gases desorbed from the BM materials were higher than those from the HG materials.

The amounts of oxygen-containing functionalities, CO_x (CO and CO_2), and ASAs of the HG and BM materials are shown in Figure 4e-f and Table 1. All of the HG materials showed low proportions of CO_x groups, with a slightly higher amount for CP-HG (Figure 4e); in terms of active surface areas, the ASAs of all HG materials were low, with values of 1.1, 0.5 and 0.6 m^2 g^{-1} for C-HG, CP-HG and P-HG, respectively. This was consistent with studies reported in the literature in which HC showed a higher ASA than graphite[25,44].

The amount of CO_x groups and the ASAs of the BM materials were considerably higher than those of the HG materials, with more for the chitosan-derived samples (15, 10 and 2 m^2 g^{-1} for C-BM, CP-BM, and P-BM, respectively). The ball milling conditions increased the proportions of oxygen functional groups on the surfaces of the materials and created many defects, as shown

by the active surface areas. These amounts varied with the type of material and were, for instance, lower in the case of the pitch material (P-HG/P-BM) than in the case of the chitosan materials (C-HG/C-BM), likely due to the more organized and rigid structure of soft carbon compared to that of hard carbon. The oxygen contents, the specific surface areas, and the impurities present in the materials contributed to larger values as well, as for the BM materials.

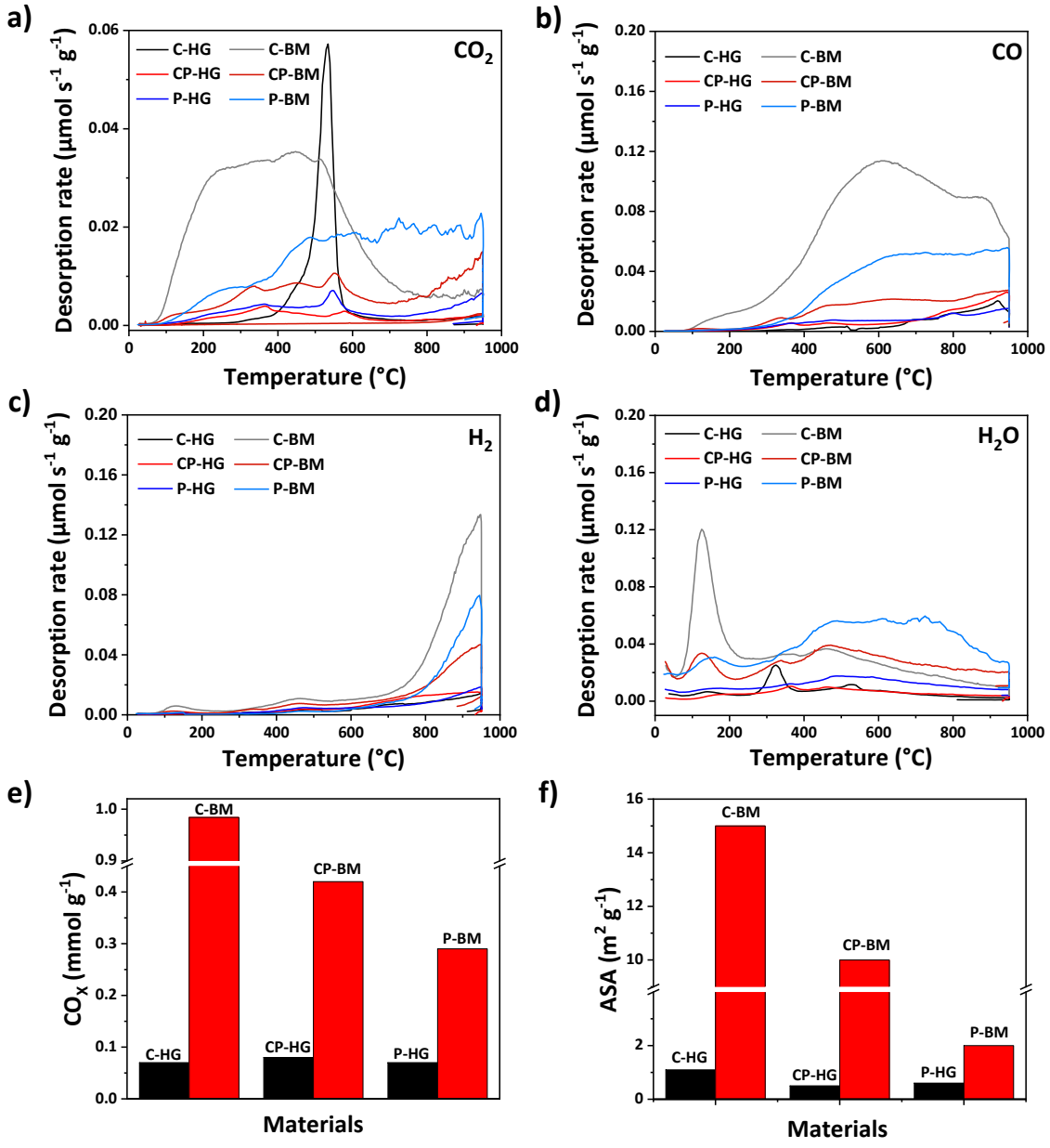

Figure 4: Desorbed gases evolved during TPD-MS analyses of the HG and BM materials: (a) CO_2, (b) CO, (c) H_2, and (d) H_2O; (e) and (f) the amounts of CO_x groups and the ASAs of the HG and BM materials.

It should be mentioned that the ASAs were not quantified in the literature, especially for the carbon materials used in KIBs, whereas they were studied for the hard carbon materials used in NIBs[38]. A small amount of CO_x groups increases the wettability of carbon with the electrolyte; however, a large quantity might lead to irreversible storage of K ions due to electrolyte decomposition, resulting in SEI formation and a high irreversible capacity in the first cycle. The defects and active sites could also be involved in the storage of K ions, leading to irreversible capacity, as observed for the hard carbons and graphite used in NIBs and LIBs [35,38,44].

3.1 Electrochemical performance

Galvanostatic profiles for the 1st charge/discharge cycles of (a) the HG materials (C-HG, CP-HG and P-HG) and (b) the BM materials (C-BM, CP-BM and P-BM) during the 1st cycle at a C/10 rate are shown in Figure 5a-b. The curves presented two distinct regions: a sloping region from 2.0 to ~0.7 V for the BM materials and from 2.0 to ~0.65 V for the HG materials, then a plateau-like region from 0.7 to 0.01 V for the BM materials and from 0.65 to 0.01 V for the HG materials. The first plateau region was wider and better defined for the HG materials. In contrast, the BM materials exhibited higher slope regions; generally, the sloping regions of KIBs are attributed to the adsorption of K ions in the defects and edge sites (capacitive behaviour), while the plateau region is related to K ion intercalation between the graphene planes and/or filling of the closed pores (faradic mechanism)[45]. It is worth mentioning that association of the sloping and plateau regions with precise mechanisms is still debated. Different studies[46,47] suggested simultaneous K-ion adsorption/intercalation mechanisms, indicating a pseudocapacitive mechanism.

Based on the different ratios for the sloping regions/plateaus in the galvanostatic curves, the capacities of the materials varied. The initial charge/discharge capacities and ICEs of the HG and BM materials are reported in Table 2.

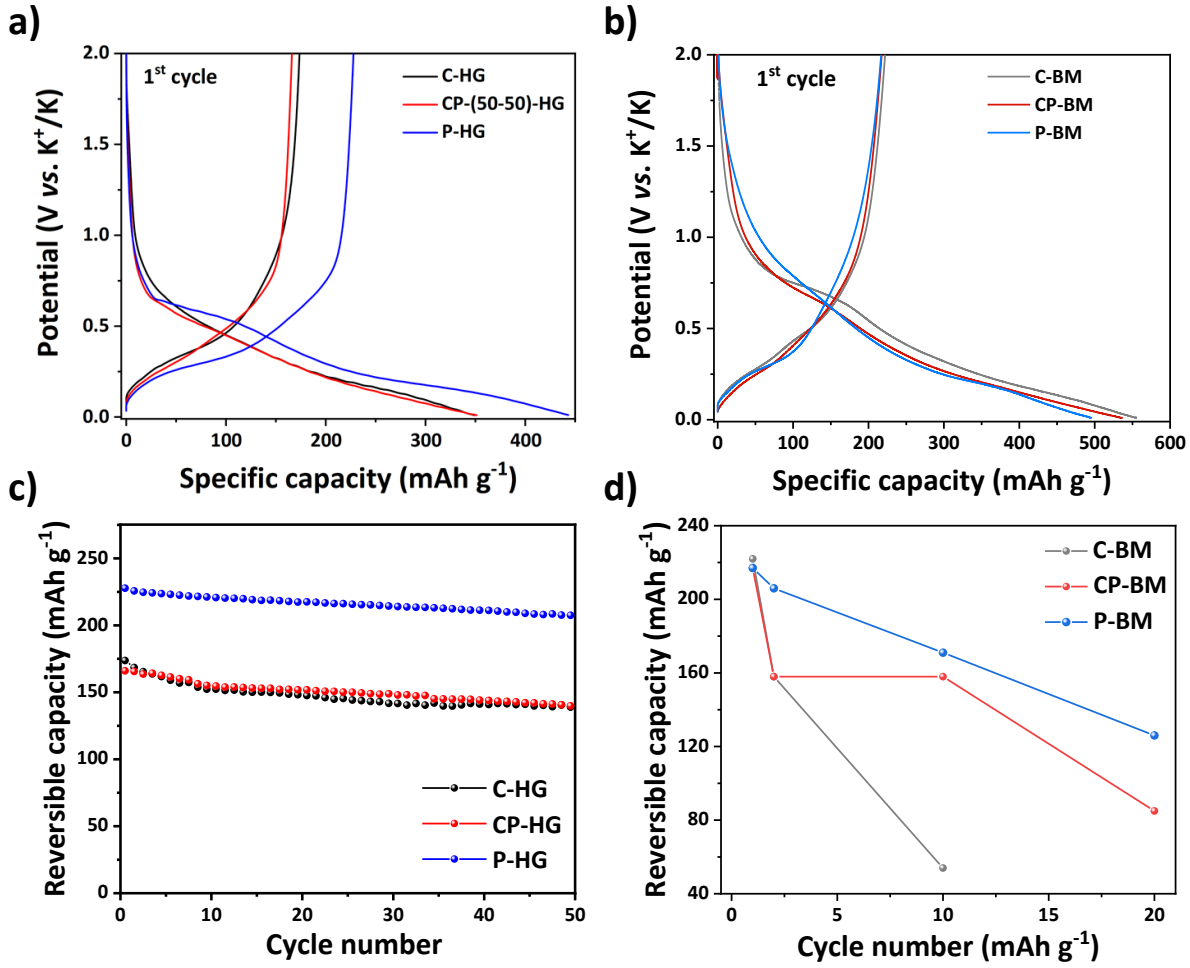

Figure 5: Galvanostatic profiles for the 1st charge/discharge cycles at 23 mA g^{-1} (C/10) of (a) the HG materials (C-HG, CP-HG and P-HG) and (b) the BM materials (C-BM, CP-BM and P-BM); (c) reversible capacity evolution during 50 cycles with the HG materials and d) during 10 to 20 cycles for C-BM, CP-BM and P-BM.

Table 2: Electrochemical characteristics of the HG and BM materials, including ICEs, first charge capacities, first discharge capacities and capacity retention rates after 10 and 50 cycles at C/10 (23 mA g^{-1}) .

	Hand ground			**Ball milled**		
Materials	**C-HG**	**CP-HG**	**P-HG**	**C-BM**	**CP-BM**	**P-BM**
ICE (%)	49	47	51	40	40	43
1st charge capacity (mAh g^{-1})	173	166	227	222	217	217
1st discharge capacity (mAh g^{-1})	349	351	443	555	537	497
Capacity retention after 10 cycles (%)	88	93	97	24	70	78
Capacity retention (%)	79*	83*	91*	24**	73**	78 **

***- after 50 cycles; **- after 10 cycles**

The HG materials exhibited reversible capacities of 173, 166 and 227 mAh g^{-1} for C-HG, CP-HG, and P-HG, respectively. These values are in the same range as the reported work on HC and SC materials in the literature as can be seen in Table S3**,** especially for low-cost carbon-based materials which are not doped by other elements. In the case of doped materials[48–51], the discharge capacities are higher due to the favoured interactions of heteroatoms/functional groups with the electrolyte, however, the charge capacity is significantly much lower, leading to iCE less than 50%. Indeed, the BM materials that possess a higher amount of O-functionalities also result in a higher discharge capacity and lower iCE than the HG materials.

The capacities increased with increasing structural organization of the carbon (Table 2 and Figure 5a) and were associated with moderate d_{002} values (still higher than that of graphite, 3.35 Å). Closed pores did not appear to enable K storage, as P-HG had the highest capacity but the lowest closed pore ratio (Table 1). A small part of the capacity may have come from the sloping region due to the interactions between K^+ and the active sites, defects, and surface functional groups; however, the low values for these materials suggested limited contributions. It is also worth to mention that the capacities of both C-HG and CP-HG may be influenced by the presence of impurities in chitosan precursor and better capacities can be obtained with a better quality of this product.

In addition, it is worth to mention that the carbon-based properties are also influenced by the slurry preparation which includes another step of ball milling. The changes on the carbon-based properties (morphology, structure, texture and surface chemistry) can influence the electrochemical performance (ICE, capacity, capacity retention…). Although the impact of this step performed in liquid organic medium can be less significant than in air conditions, its influence might explain why a clear tendency between physico-chemical properties to electrochemical performance, especially for the HG-materials, is not observed. This influence of the slurry preparation step can be seen by comparing the SEM images of the HG-materials (Figure 1a-c) and the corresponding electrodes after the second step of ball milling for the slurry preparation (Figure S6a-c). We can notice that this step induces the particle size decrease of the HG-materials, even though the slurry was prepared in a liquid medium (NMP) using a smooth conditions (lower rotation speed (200 rpm vs 500 rpm)). Furthermore, this step might influence also the structure, texture and surface chemistry.

On the other hand, the BM materials showed very similar charge capacities of 222 (C-BM), 217 (CP-BM) and 217 (P-BM) mAh g^{-1} after the first cycle, which were higher than those of the

HG materials (Table 2 and Figure 5b). For these materials, the sloping contribution to the capacity was higher and was related to the surface properties (active sites, functional groups, surface area, etc.). However, the capacities faded drastically after the first cycle, as shown in Figure S7, mainly due to SEI formation arising from electrolyte decomposition on the surface of the electrode, as well as K^+ trapping in the structure and/or pores[52,53]. This was consistent with the low ICEs of the BM materials, e.g., 40 (C-BM), 40 (CP-BM), and 43% (P-BM) vs. those of the HGs, e.g., 49 (C-HG), 47 (CP-HG) and 51% (P-BM). The obtained ICEs of the HG materials are in the same line as the ICEs reported in the literature (Table S3), although the comparison still difficult to realise since different electrode formulations are used. This parameter is also considered as a critical point since different carbon-based materials (graphite, HC, SC, doped carbons) were studied in the literature and the ICE values generally do not exceed 65%. This means that a more fundamental understanding is needed, especially in terms of electrodes formulation, electrolyte type, SEI formation, and K^+ storage mechanisms, etc. Improving the ICE involves careful attention to various factors. This includes the powder grinding conditions optimization and the control of the carbon-based materials properties (morphology, structure, texture, surface chemistry and defects), as discussed in this work. Furthermore, the formulation of the slurry comprising binder and additive type [54–56] as well as its preparation process, play crucial roles in maintaining the initial carbon properties and enhancing the electrode performance, thereby improving ICE. Additionally, the choice of salt, solvent, and additives in the electrolyte impacts the stability of SEI layer, affecting the ICE[57–59]. Calendaring of electrodes, both for half and full cells, is also fundamental in achieving better ICE [3]. In the case of full cells, the ICE can be influenced by the mass ratio between positive and negative electrodes, as well as their respective working potentials. Consequently, all these parameters still need to be optimised for enhancing the ICE to meet the criteria for practical application. Furthermore, the formation of the SEI was not related to the material

properties alone, since the HG materials with low SSAs, ASAs and CO_x proportions and large d_{002} spacings also showed low ICEs (Table 2). Indeed, SEI formation impacted the performance of the half cells, and the high reactivity of potassium metal is expected to cause substantial electrolyte degradation on the surfaces.

It was demonstrated in the literature[25,60,61] that higher coulombic efficiencies and better passivation of the working electrode were realised with other electrolytes, such as 0.8 M KFSI in EC:DEC, compared to 0.8 M KPF_6 in EC. Therefore, special attention must be paid to the electrolyte choice. Another factor, as mentioned below, is the highly reactive nature of K metal. The SEI formed on the K metal surface due to simple contact with the 0.8 M KFSI EC:DEC was shown to be largely inorganic material (60 at.%), but with 0.8 M KPF_6 EC:DEC, it was predominantly organic (90 at.%)[62]. The organic SEI layer could be less stable during cycling.

Indeed, for the BM materials, poor cycling performance was observed after the first (Figure 5d, Figure S7 and Table 2), with enormous capacity losses and a low-capacity retention rates (after 10 cycles) of 24, 73 and 78% for C-BM, CP-BM and P-BM, respectively. These poor electrochemical data were associated with changes in the properties, and were in particular related to the SSAs, CO_X groups, ASAs and the presence of impurities after ball milling, as reported in the literature[5].

On the other hand, the HG materials displayed better cycling performance for up to 50 cycles (Figure 5c and Figure S8), and high capacity retention rates (50 cycles) were exhibited by all of the HG materials, particularly the P-HG sample (91%), followed by the CP-HG (83%) and the C-HG (79%) samples (Table 2). XPS analyses was used to correlate the electrochemical performance with growth of the SEI passivation layer and to evaluate the impact of K metal on this process. Figure 6 shows XPS core level spectra (C 1s, K 2p, and O 1s) for the P-HG electrodes.

In terms of peak attribution (Figure 6a, b, c, d and Table S2), the C 1s and K 2p spectra for the soft carbon electrode showed peaks at 284.4 and 285.0 corresponding to C=C groups (carbon black and P-HG) and hydrocarbons, respectively. Furthermore, the C 1s core spectra exhibited peaks at 287, 288.5, and 289.5 eV that were attributed to CO, CO_2, and CO_3 groups, respectively. The PVDF binder showed two peaks at 286 and 290.5 eV, which were assigned to CH_2 and CF_2 groups, respectively. The K 2p peaks at 293.5 (K $2p_{3/2}$) and 296.3 (K $2p_{1/2}$) eV are assigned to KF, KOH, K_2CO_3 and ROK components (KF, K_2CO_3 and KOH). The other K 2p peaks, at 294.8 and 297.4 eV, were ascribed to $K_xP_yF_z$ (decomposition by-products from the KPF_6 electrolyte[63]). Moreover, the O 1s core spectrum showed the presence of KOH, ROK, CO_2/CO_3, and CO groups with binding energies of 529.7, 531.5, 532.7, and 533.7 eV, respectively.

If considering the electrode surface composition, comparisons of the passivation layer evolution for the pristine (Figure 6a) and assembled P-HG electrodes after 12 h of OCV and after the 1st and 5th cycles are displayed in Figure 6b, c, and d.

The P-HG passivation layers became thicker without cycling which mean that a chemical SEI layer is formed (Figure 6b), and remarkable increases were seen in the peak areas for CH, CO, KF, ROK, and $K_xP_yF_z$, indicating that more salt and solvent decomposed at the OCV due to the high reactivity of K metal[64]. By comparing the 1st (chemical and electrochemical SEI layer) and 5th cycles (electrochemical SEI layer), electrochemical cycling caused substantial degradation of the solvent, which was confirmed by the irreversible cycling capacity of the P-HG (Figure S7a) and the considerably increased areas for the CH, CO and ROK peaks. As shown in Table S2, the amounts of organic byproducts containing carbon and oxygen, as well as the smaller fractions of potassium and fluorine inorganic species, were more significant after the 5th cycle than the 1st cycle and less significant at the OCV (i.e., at the OCV, there was more solvent

degradation). Thus, the low initial coulombic efficiency and the high irreversible capacity of P-HG may have arisen from SEI growth (i.e., electrolyte decomposition); a more organic SEI appears to be impractical for desirable electrochemical performance (long-term cycling), and better electrolytes are needed to provide stable inorganic SEIs[26].

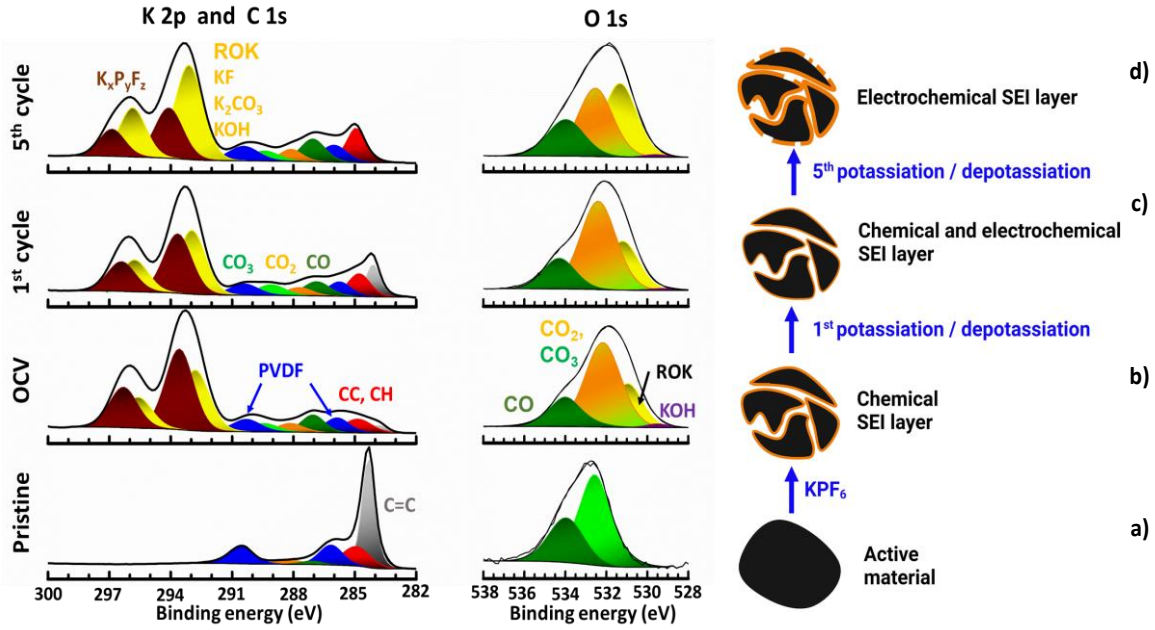

Figure 6: C 1s, K 2p, and O 1s XPS core level spectra as well as a schematic representation of the accompanying phenomena for P-HG; (a) the pristine electrode, (b) after 12 hours of OCV, (c) after the 1st and (d) the 5th cycles versus K metal. Right image was created by the authors with BioRender.com.

There is a strong demand for full K ion cells that use a real positive electrode, replacing the K metal, to achieve practical use. One of the critical factors to consider is the seamless integration of positive and negative electrode materials to ensure that all of the cells meet the energy density criteria. This is why it is of great interest to switch to full cell configuration tests[65,66].

The 3-electrode cells were used to evaluate the effects of the negative/positive (N/P) areal capacity ratio on the delivered capacity and CE. Note that the 3-electrode cells were used to identify the limiting electrode and the phenomena.

The impact of the P-HG//KVPFO/C areal capacity ratio was then evaluated with the Swagelok T cells (Figure 7). Indeed, in the first cycle (Figure 7a), the KVPFO/C and P-HG electrodes exhibited 4.8 and 0.01 V cut-off voltages with reversible capacities of 80 and 150 mAh g^{-1}, respectively, due to the optimized areal capacities (N/P=1.17) and diameter (1.16) ratios[67,68]. After 5 cycles, the P-HG electrodes delivered only 130 mAh g^{-1} and did not reach the 0.01 V cut-off voltage, which could have been due to the uncontrolled pressure in the 3-electrode T cells and/or the unoptimized electrolyte (i.e., the presence of an unsuitable organic SEI), as described in Figure 6.

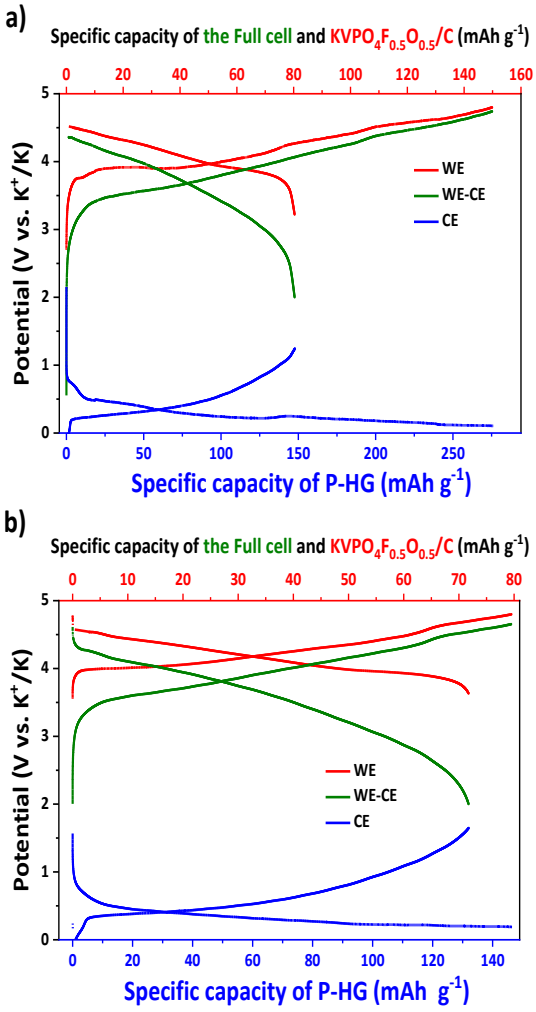

Figure 7: Galvanostatic charge/discharge profiles for a) the 1st and b) 5th cycles at C/10 over the range 2.0–4.8 V for KVPFO//P-HG 3-electrode T cells.

The same parameters will be used to investigate the electrochemical performance of the P-HG-based full cell (Scheme 2). Figures 8a-c show the capacity retention rates of the P-HG//KVPFO/C full coin-cells after application of the OCV for 12 h at 40 °C.

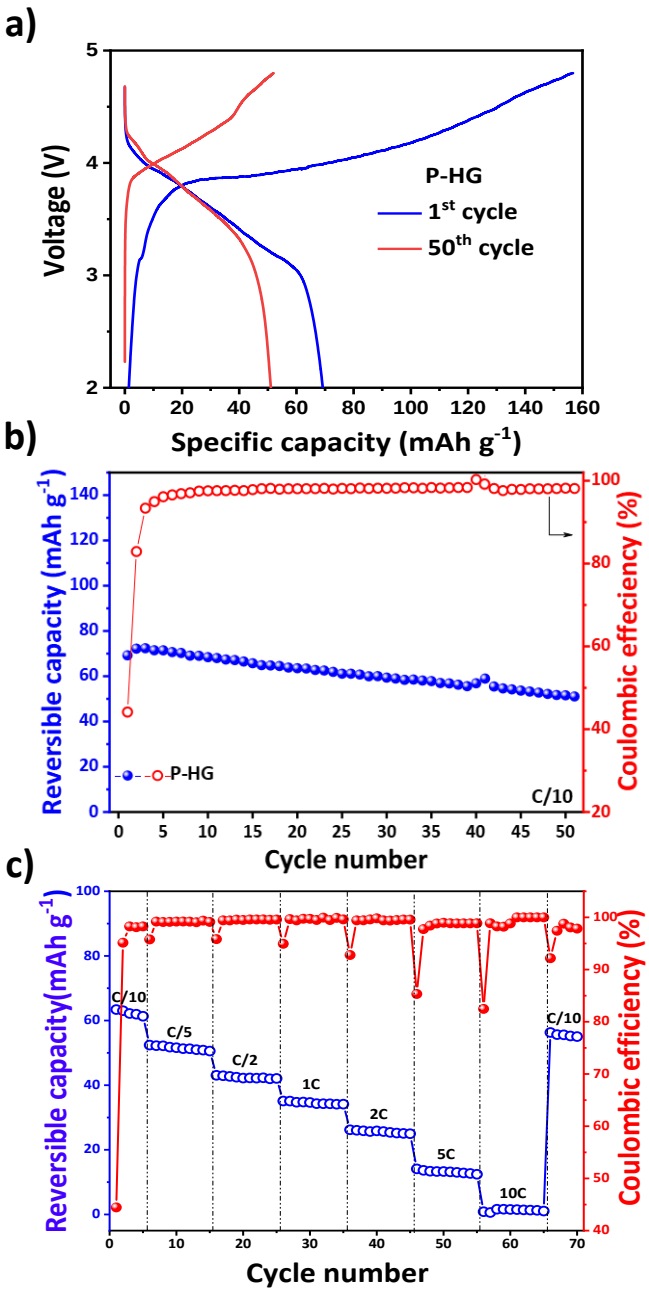

Figure 8: a) Galvanostatic charge/discharge profiles for the 1st and 50th cycles, **b)** long-term cycling and coulombic efficiency over 50 cycles and **c)** rate performance and corresponding CE over 70 cycles from C/10 to 10C with the P-HG//KVPFO/C full cell.

The cell exhibited an initial capacity and coulombic efficiency of 69 mAh $g_{KVPFO/C}^{-1}$ and 44%, respectively, with a capacity retention rate of 74% over 50 cycles. The rate performance was also studied from C/10 to 10C (Figure 8c), and the full cell delivered capacities of 64, 51, 42, 34, 26, 13, and 0 mAh g^{-1} at C/10, C/5, C/2, 1C, 2C, 5C, and 10C, respectively, as well as a capacity recovery rate of 88 after 70 cycles. This rate capability demonstrated the potential of the P-HG soft carbon for use as a negative electrode material enabling KIBs to reach high power densities (i.e., graphite cannot exceed a 1C potassiation rate)[67,69], a proof of concept can be seen in Figure S9.

In addition, it is worth mentioning that these results are comparable with the results obtained in literature [70,71] that use a pre-cyling in a half cell configuration before coupling it with a real positive electrode. This is not the case in our work; therefore, the assembly is more realistic and simple, although further optimizations are still needed.

Conclusion

Hard and soft carbon materials with different properties were synthesized from chitosan and pitch carbon precursors as well as a mixture. The impacts of hand grinding and ball milling on the physicochemical properties and the electrochemical performance were studied. The morphologies, structures, textures, and surface chemistries of the materials were affected. The use of mechanical grinding led to smaller and more suitable particle sizes and homogeneous electrode materials. However, the specific surface areas, the proportion of oxygenated groups, and the number of defects were considerably higher for the BM materials compared to the HG materials. These modifications were more significant for materials with more disordered structures and oxygen functional groups (hard carbons) prepared from chitosan. The changes in the carbon properties seen after ball milling directly affected the electrochemical performance vs. K-metal. Therefore, the ICEs of the BM materials were lower than those of the hand ground materials. Generally, the ICE values were very low, with a maximum of 51%; this was explained by the SEI passivation layer composition studied by XPS, which highlighted the predominantly organic nature of the layer. The interactions between the electrodes and the electrolyte, especially with K metal used as the counter electrode, were responsible for SEI formation. Moreover, the BM materials showed enormous decreases in their capacities starting after the first cycle, while the hand ground materials presented good stability during cycling and preserved capacity retention rates up to 91% after 50 cycles (pitch-based soft carbon). The best performance was found for pitch-based soft carbon (P-HG), which combined a suitable structure (large interlayer spacings) and surface properties (low values). A full cell was constructed with P-HG and $KVPO_4F_{0.5}O_{0.5}$/C, and a promising performance was obtained (capacity of 69 mAh $g_{KVPFO/C}^{-1}$ and an ICE of 44%). Furthermore, when tested at different C-rates, the P-HG showed stable cycling even at high C-rates, while graphite cannot withstand

potassiation rates of more than 1C. In summary, this work highlighted the importance of electrode processing and the need to preserve the material properties to maintain the desired electrochemical performance.

Conflict of Interest

The authors declare no conflicts of interest.

Supporting information

TGA curves of the initial precursors; images of pitch precursor after a heat treatment; pore size distribution of all materials; helium density of all materials; XPS chemical composition and wide scan of the HG materials; long-term cycling of all materials; amount of surface functional groups of postmortem carbon electrodes by XPS.

Acknowledgements

This work was financially supported through the Algerian Ministry of High Education and Scientific Research. The authors are grateful for financial support for electrochemical test realization through the TROPIC project supported by Agence Nationale de la Recherche (ANR), Grant ANR-19-CE05-0026.

The authors thank the technical staff of the "Carbon and Hybrid Material" team (Bénédicte Réty and Adrian Beda) for their daily support with the fabrication and analyses of carbon materials. The authors thank Dr. Laurence Croguennec and Romain Wernert from ICMCB for providing the pristine positive electrode material used in this work. The authors thank Dr. Loïc Vidal (HRTEM images) and Dr. Jean-Marc Le Meins (XRD data) for technical support with the IS2M technical platforms. The authors thank the technical staff of ICGM for their experimental help.

References

(1) Yang, J.; Zhai, Y.; Zhang, X.; Zhang, E.; Wang, H.; Liu, X.; Xu, F.; Kaskel, S. Perspective on Carbon Anode Materials for K^+ Storage: Balancing the Intercalation-Controlled and Surface-Driven Behavior. *Adv. Energy Mater.* **2021**, *11* (29), 2100856. https://doi.org/10.1002/aenm.202100856.

(2) Zhang, C.; Zhao, H.; Lei, Y. Recent Research Progress of Anode Materials for Potassium-ion Batteries. *ENERGY Environ. Mater.* **2020**, *3* (2), 105–120. https://doi.org/10.1002/eem2.12059.

(3) Beda, A.; Rabuel, F.; Morcrette, M.; Knopf, S.; Taberna, P.-L.; Simon, P.; Matei Ghimbeu, C. Hard Carbon Key Properties Allow for the Achievement of High Coulombic Efficiency and High Volumetric Capacity in Na-Ion Batteries. *J. Mater. Chem. A* **2021**, *9* (3), 1743–1758. https://doi.org/10.1039/D0TA07687B.

(4) Escamilla-Pérez, A. M.; Roland, A.; Giraud, S.; Guiraud, C.; Virieux, H.; Demoulin, K.; Oudart, Y.; Louvain, N.; Monconduit, L. Pitch-Based Carbon/Nano-Silicon Composite, an Efficient Anode for Li-Ion Batteries. *RSC Adv.* **2019**, *9* (19), 10546–10553. https://doi.org/10.1039/C9RA00437H.

(5) Conder, J.; Vaulot, C.; Marino, C.; Villevieille, C.; Ghimbeu, C. M. Chitin and Chitosan—Structurally Related Precursors of Dissimilar Hard Carbons for Na-Ion Battery. *ACS Appl. Energy Mater.* **2019**, *2* (7), 4841–4852. https://doi.org/10.1021/acsaem.9b00545.

(6) Liu, Y.; Lu, Y.; Xu, Y.; Meng, Q.; Gao, J.; Sun, Y.; Hu, Y.; Chang, B.; Liu, C.; Cao, A. Pitch-Derived Soft Carbon as Stable Anode Material for Potassium Ion Batteries. *Adv. Mater.* **2020**, *32* (17), 2000505. https://doi.org/10.1002/adma.202000505.

(7) Zhao, Y.; Cong, Y.; Ning, H.; Fei, X.; Wu, C.; Wang, H.; He, Z.; Wang, Y.; Zhao, Q.; Wu, M. N, P Co-Doped Pitch Derived Soft Carbon Nanoboxes as High-Performance Anodes for Sodium-Ion Batteries. *J. Alloys Compd.* **2022**, *918*, 165691. https://doi.org/10.1016/j.jallcom.2022.165691.

(8) Jian, Z.; Hwang, S.; Li, Z.; Hernandez, A. S.; Wang, X.; Xing, Z.; Su, D.; Ji, X. Hard–Soft Composite Carbon as a Long-Cycling and High-Rate Anode for Potassium-Ion Batteries. *Adv. Funct. Mater.* **2017**, *27* (26), 1700324. https://doi.org/10.1002/adfm.201700324.

(9) Carboni, M.; Manzi, J.; Armstrong, A. R.; Billaud, J.; Brutti, S.; Younesi, R. Analysis of the Solid Electrolyte Interphase on Hard Carbon Electrodes in Sodium-Ion Batteries. *ChemElectroChem* **2019**, *6* (6), 1745–1753. https://doi.org/10.1002/celc.201801621.

(10) Bonino, F.; Brutti, S.; Piana, M.; Natale, S.; Scrosati, B.; Gherghel, L.; Müllen, K. Structural and Electrochemical Studies of a Hexaphenylbenzene Pyrolysed Soft Carbon as Anode Material in Lithium Batteries. *Electrochimica Acta* **2006**, *51* (17), 3407–3412. https://doi.org/10.1016/j.electacta.2005.09.036.

(11) Ilic, I. K.; Schutjajew, K.; Zhang, W.; Oschatz, M. Changes of Porosity of Hard Carbons during Mechanical Treatment and the Relevance for Sodium-Ion Anodes. *Carbon* **2022**, *186*, 55–63. https://doi.org/10.1016/j.carbon.2021.09.063.

(12) Yue, X.; Wang, H.; Wang, S.; Zhang, F.; Zhang, R. In-Plane Defects Produced by Ball-Milling of Expanded Graphite. *J. Alloys Compd.* **2010**, *505* (1), 286–290. https://doi.org/10.1016/j.jallcom.2010.06.048.

(13) Zhang, W.; Yan, Y.; Xie, Z.; Yang, Y.; Xiao, Y.; Zheng, M.; Hu, H.; Dong, H.; Liu, Y.; Liang, Y. Engineering of Nanonetwork-Structured Carbon to Enable High-Performance Potassium-Ion Storage. *J. Colloid Interface Sci.* **2020**, *561*, 195–202. https://doi.org/10.1016/j.jcis.2019.11.042.

(14) Sun, Q.; Li, D.; Cheng, J.; Dai, L.; Guo, J.; Liang, Z.; Ci, L. Nitrogen-Doped Carbon Derived from Pre-Oxidized Pitch for Surface Dominated Potassium-Ion Storage. *Carbon* **2019**, *155*, 601–610. https://doi.org/10.1016/j.carbon.2019.08.059.

(15) Lin, X.; Liu, Y.; Tan, H.; Zhang, B. Advanced Lignin-Derived Hard Carbon for Na-Ion Batteries and a Comparison with Li and K Ion Storage. *Carbon* **2020**, *157*, 316–323. https://doi.org/10.1016/j.carbon.2019.10.045.

(16) Wang, Q.; Gao, C.; Zhang, W.; Luo, S.; Zhou, M.; Liu, Y.; Liu, R.; Zhang, Y.; Wang, Z.; Hao, A. Biomorphic Carbon Derived from Corn Husk as a Promising Anode Materials for Potassium Ion Battery. *Electrochimica Acta* **2019**, *324*, 134902. https://doi.org/10.1016/j.electacta.2019.134902.

(17) Ponrouch, A.; Palacín, M. R. On the Impact of the Slurry Mixing Procedure in the Electrochemical Performance of Composite Electrodes for Li-Ion Batteries: A Case Study for Mesocarbon Microbeads (MCMB) Graphite and Co3O4. *J. Power Sources* **2011**, *196* (22), 9682–9688. https://doi.org/10.1016/j.jpowsour.2011.07.045.

(18) Tan, H.; Zhou, R.; Zhang, B. Understanding Potassium Ion Storage Mechanism in Pitch-Derived Soft Carbon and the Consequence on Cyclic Stability. *J. Power Sources* **2021**, *506*, 230179. https://doi.org/10.1016/j.jpowsour.2021.230179.

(19) Larbi, L.; Larhrib, B.; Beda, A.; Madec, L.; Monconduit, L.; Matei Ghimbeu, C. Impact of Hard Carbon Properties on Their Performance in Potassium-Ion Batteries. *ACS Appl. Energy Mater.* **2023**, *6* (10), 5274–5289. https://doi.org/10.1021/acsaem.3c00201.

(20) Hua-jun, G.; Xin-hai, L.; Xin-ming, Z.; Hong-qiang, W.; Zhi-xing, W.; Wen-jie, P. Diffusion Coefficient of Lithium in Artificial Graphite, Mesocarbon Microbeads, and Disordered Carbon. *New Carbon Mater.* **2007**. https://doi.org/10.1016/S1872-5805(07)60006-7

(21) Short, M. A.; Walker, P. L. Measurement of Interlayer Spacings and Crystal Sizes in Turbostratic Carbons. *Carbon* **1963**, *1* (1), 3–9. https://doi.org/10.1016/0008-6223(63)90003-4.

(22) Fujimoto, M.; Kano, A.; Nobuhiko, H. Negative-electrode active material for sodium-ion secondary battery, method for the manufacturing said negative-electrode active material, and sodium ion secondary battery. Patent WO/2014/88723, 2014.

(23) Brender, P.; Gadiou, R.; Rietsch, J.-C.; Fioux, P.; Dentzer, J.; Ponche, A.; Vix-Guterl, C. Characterization of Carbon Surface Chemistry by Combined Temperature Programmed Desorption with in Situ X-Ray Photoelectron Spectrometry and Temperature Programmed Desorption with Mass Spectrometry Analysis. *Anal. Chem.* **2012**, *84* (5), 2147–2153. https://doi.org/10.1021/ac102244b.

(24) Matei Ghimbeu, C.; Górka, J.; Simone, V.; Simonin, L.; Martinet, S.; Vix-Guterl, C. Insights on the Na+ Ion Storage Mechanism in Hard Carbon: Discrimination between the Porosity, Surface Functional Groups and Defects. *Nano Energy* **2018**, *44*, 327–335. https://doi.org/10.1016/j.nanoen.2017.12.013.

(25) Larbi, L.; Larhrib, B.; Beda, A.; Madec, L.; Monconduit, L.; Matei Ghimbeu, C. Impact of Hard Carbon Properties on Their Performance in Potassium-Ion Batteries. *ACS Appl. Energy Mater.* **2023**, acsaem.3c00201. https://doi.org/10.1021/acsaem.3c00201.

(26) Caracciolo, L.; Madec, L.; Martinez, H. XPS Analysis of K-Based Reference Compounds to Allow Reliable Studies of Solid Electrolyte Interphase in K-Ion Batteries. *ACS Appl. Energy Mater.* **2021**, *4* (10), 11693–11699. https://doi.org/10.1021/acsaem.1c02400.

(27) Wernert, R.; Nguyen, L. H. B.; Iadecola, A.; Weill, F.; Fauth, F.; Monconduit, L.; Carlier, D.; Croguennec, L. Self-Discharge Mechanism of High-Voltage $KVPO_4F$ for K-Ion

Batteries. *ACS Appl. Energy Mater.* **2022**, *5* (12), 14913–14921. https://doi.org/10.1021/acsaem.2c02379.

(28) Larbi, L.; Wernert, R.; Fioux, P.; Croguennec, L.; Monconduit, L.; Matei Ghimbeu, C. Enhanced Performance of $KVPO_4F_{0.5}O_{0.5}$ in Potassium Batteries by Carbon Coating Interfaces. *ACS Appl. Mater. Interfaces* **2023**, *15* (15), 18992–19001. https://doi.org/10.1021/acsami.3c01240.

(29) Wernert, R.; Nguyen, L. H. B.; Petit, E.; Camacho, P. S.; Iadecola, A.; Longo, A.; Fauth, F.; Stievano, L.; Monconduit, L.; Carlier, D.; Croguennec, L. Controlling the Cathodic Potential of $KVPO_4F$ through Oxygen Substitution. *Chem. Mater.* **2022**, *34* (10), 4523–4535. https://doi.org/10.1021/acs.chemmater.2c00295.

(30) Larhrib, B.; Madec, L. Toward Highly Reliable Potassium-Ion Half and Full Coin Cells. *Batter. Supercaps* **2023**, *6* (5), e202300061. https://doi.org/10.1002/batt.202300061.

(31) Liu, Z.; Guo, X.; Shi, L.; He, W.; Wu, J.; Liu, Q.; Liu, J. Reaction of Volatiles – A Crucial Step in Pyrolysis of Coals. *Fuel* **2015**, *154*, 361–369. https://doi.org/10.1016/j.fuel.2015.04.006.

(32) Sansom, J. A. The Stabilisation Process in Mesophase Pitch Based Carbon Materials (2008); PhD thesis, University of Leeds.

(33) Wrogemann, J. M.; Fromm, O.; Deckwirth, F.; Beltrop, K.; Heckmann, A.; Winter, M.; Placke, T. Impact of Degree of Graphitization, Surface Properties and Particle Size Distribution on Electrochemical Performance of Carbon Anodes for Potassium-Ion Batteries. *Batter. Supercaps* **2022**, *5* (6). https://doi.org/10.1002/batt.202200045.

(34) Tillmans, H. Carbonization of Pitch. *Fuel* **1985**, *64* (9), 1197–1203. https://doi.org/10.1016/0016-2361(85)90174-7.

(35) Beda, A.; Rabuel, F.; Morcrette, M.; Knopf, S.; Taberna, P.-L.; Simon, P.; Matei Ghimbeu, C. Hard Carbon Key Properties Allow for the Achievement of High Coulombic Efficiency and High Volumetric Capacity in Na-Ion Batteries. *J. Mater. Chem. A* **2021**, *9* (3), 1743–1758. https://doi.org/10.1039/D0TA07687B.

(36) Crystallite Growth in Graphitizing and Non-Graphitizing Carbons. *Proc. R. Soc. Lond. Ser. Math. Phys. Sci.* **1951**, *209* (1097), 196–218. https://doi.org/10.1098/rspa.1951.0197.

(37) Wang, B.; Zhang, Z.; Yuan, F.; Zhang, D.; Wang, Q.; Li, W.; Li, Z.; Wu, Y. A.; Wang, W. An Insight into the Initial Coulombic Efficiency of Carbon-Based Anode Materials for Potassium-Ion Batteries. *Chem. Eng. J.* **2022**, *428*, 131093. https://doi.org/10.1016/j.cej.2021.131093.

(38) Beda, A.; Vaulot, C.; Rabuel, F.; Morcrette, M.; Matei Ghimbeu, C. The Role of Specific and Active Surface Areas in Optimizing Hard Carbon Irreversible Capacity Loss in Sodium Ion Batteries. *Energy Adv.* **2022**, *1* (4), 185–190. https://doi.org/10.1039/D2YA00004K.

(39) Nasrullah, A.; Khan, A. S.; Bhat, A. H.; Din, I. U.; Inayat, A.; Muhammad, N.; Bakhsh, E. M.; Khan, S. B. Effect of Short Time Ball Milling on Physicochemical and Adsorption Performance of Activated Carbon Prepared from Mangosteen Peel Waste. *Renew. Energy* **2021**, *168*, 723–733. https://doi.org/10.1016/j.renene.2020.12.077.

(40) Harindintwali, J. D.; He, C.; Xiang, L.; Dou, Q.; Liu, Y.; Wang, M.; Wen, X.; Fu, Y.; Islam, M. U.; Chang, S. X.; Kueppers, S.; Shaheen, S. M.; Rinklebe, J.; Jiang, X.; Schaeffer, A.; Wang, F. Effects of Ball Milling on Biochar Adsorption of Contaminants in Water: A Meta-Analysis. *Sci. Total Environ.* **2023**, *882*, 163643. https://doi.org/10.1016/j.scitotenv.2023.163643.

(41) Figueiredo, J. L.; Pereira, M. F. R.; Freitas, M. M. A.; Órfão, J. J. M. Modification of the Surface Chemistry of Activated Carbons. *Carbon* **1999**, *37* (9), 1379–1389. https://doi.org/10.1016/S0008-6223(98)00333-9.

(42) Beda, A.; Taberna, P.-L.; Simon, P.; Matei Ghimbeu, C. Hard Carbons Derived from Green Phenolic Resins for Na-Ion Batteries. *Carbon* **2018**, *139*, 248–257. https://doi.org/10.1016/j.carbon.2018.06.036.

(43) Moussa, G.; Matei Ghimbeu, C.; Taberna, P.-L.; Simon, P.; Vix-Guterl, C. Relationship between the Carbon Nano-Onions (CNOs) Surface Chemistry/Defects and Their Capacitance in Aqueous and Organic Electrolytes. *Carbon* **2016**, *105*, 628–637. https://doi.org/10.1016/j.carbon.2016.05.010.

(44) Ghimbeu, C. M.; Decaux, C.; Brender, P.; Dahbi, M.; Lemordant, D.; Raymundo-Piñero, E.; Anouti, M.; Béguin, F.; Vix-Guterl, C. Influence of Graphite Characteristics on the Electrochemical Performance in Alkylcarbonate LiTFSI Electrolyte for Li-Ion Capacitors and Li-Ion Batteries. *J. Electrochem. Soc.* **2013**, *160* (10), A1907–A1915. https://doi.org/10.1149/2.101310jes.

(45) Lei, H.; Li, J.; Zhang, X.; Ma, L.; Ji, Z.; Wang, Z.; Pan, L.; Tan, S.; Mai, W. A Review of Hard Carbon Anode: Rational Design and Advanced Characterization in Potassium Ion Batteries. *InfoMat* **2022**, *4* (2). https://doi.org/10.1002/inf2.12272.

(46) Chen, C.; Wu, M.; Wang, Y.; Zaghib, K. Insights into Pseudographite-Structured Hard Carbon with Stabilized Performance for High Energy K-Ion Storage. *J. Power Sources* **2019**, *444*, 227310. https://doi.org/10.1016/j.jpowsour.2019.227310.

(47) Xu, J.; Fan, C.; Ou, M.; Sun, S.; Xu, Y.; Liu, Y.; Wang, X.; Li, Q.; Fang, C.; Han, J. Correlation between Potassium-Ion Storage Mechanism and Local Structural Evolution in Hard Carbon Materials. *Chem. Mater.* **2022**, *34* (9), 4202–4211. https://doi.org/10.1021/acs.chemmater.2c00646.

(48) Liu, C.; Zheng, H.; Yu, K.; Feng, D.; Li, H.; Yao, J.; Zhang, X.; Ma, T.; Qiu, J. Direct Synthesis of P/O-Enriched Pitch-Based Carbon Microspheres from a Coordinated Emulsification and Pre-Oxidation towards High-Rate Potassium-Ion Batteries. *Carbon* **2022**, *194*, 176–184. https://doi.org/10.1016/j.carbon.2022.03.064.

(49) Liu, C.; Xiao, N.; Li, H.; Dong, Q.; Wang, Y.; Li, H.; Wang, S.; Zhang, X.; Qiu, J. Nitrogen-Doped Soft Carbon Frameworks Built of Well-Interconnected Nanocapsules Enabling a Superior Potassium-Ion Batteries Anode. *Chem. Eng. J.* **2020**, *382*, 121759. https://doi.org/10.1016/j.cej.2019.05.120.

(50) Liu, Q.; Han, F.; Zhou, J.; Li, Y.; Chen, L.; Zhang, F.; Zhou, D.; Ye, C.; Yang, J.; Wu, X.; Liu, J. Boosting the Potassium-Ion Storage Performance in Soft Carbon Anodes by the Synergistic Effect of Optimized Molten Salt Medium and N/S Dual-Doping. *ACS Appl. Mater. Interfaces* **2020**, *12* (18), 20838–20848. https://doi.org/10.1021/acsami.0c00679.

(51) Lu, X.; Zhou, J.; Huang, L.; Peng, H.; Xu, J.; Liu, G.; Shi, C.; Sun, Z. Low-Temperature Carbonized N/O/S-Tri-Doped Hard Carbon for Fast and Stable K-Ions Storage. *Adv. Energy Mater.* **2024**, *14* (4), 2303081. https://doi.org/10.1002/aenm.202303081.

(52) Touja, J.; Gabaudan, V.; Farina, F.; Cavaliere, S.; Caracciolo, L.; Madec, L.; Martinez, H.; Boulaoued, A.; Wallenstein, J.; Johansson, P.; Stievano, L.; Monconduit, L. Self-Supported Carbon Nanofibers as Negative Electrodes for K-Ion Batteries: Performance and Mechanism. *Electrochimica Acta* **2020**, *362*, 137125. https://doi.org/10.1016/j.electacta.2020.137125.

(53) Wang, H.; Zhai, D.; Kang, F. Solid Electrolyte Interphase (SEI) in Potassium Ion Batteries. *Energy Environ. Sci.* **2020**, *13* (12), 4583–4608. https://doi.org/10.1039/D0EE01638A.

(54) Wu, X.; Xing, Z.; Hu, Y.; Zhang, Y.; Sun, Y.; Ju, Z.; Liu, J.; Zhuang, Q. Effects of Functional Binders on Electrochemical Performance of Graphite Anode in Potassium-Ion Batteries. *Ionics* **2019**, *25* (6), 2563–2574. https://doi.org/10.1007/s11581-018-2763-4.

(55) Liu, W.; Liu, W.; Jiang, Y.; Gui, Q.; Ba, D.; Li, Y.; Liu, J. Binder-Free Electrodes for Advanced Potassium-Ion Batteries: A Review. *Chin. Chem. Lett.* **2021**, *32* (4), 1299–1308. https://doi.org/10.1016/j.cclet.2020.08.032.

(56) Larhrib, B.; Madec, L.; Monconduit, L.; Martinez, H. Optimized Electrode Formulation for Enhanced Performance of Graphite in K-Ion Batteries. *Electrochimica Acta* **2022**, *425*, 140747. https://doi.org/10.1016/j.electacta.2022.140747.

(57) Wu, Z.; Zou, J.; Shabanian, S.; Golovin, K.; Liu, J. The Roles of Electrolyte Chemistry in Hard Carbon Anode for Potassium-Ion Batteries. *Chem. Eng. J.* **2022**, *427*, 130972. https://doi.org/10.1016/j.cej.2021.130972.

(58) Han, Y.; Vijaya Kumar Saroja, A. P.; Tinker, H. R.; Xu, Y. Interphases in the Electrodes of Potassium Ion Batteries. *J. Phys. Mater.* **2022**, *5* (2), 022001. https://doi.org/10.1088/2515-7639/ac5dce.

(59) Wang, H.; Zhai, D.; Kang, F. Solid Electrolyte Interphase (SEI) in Potassium Ion Batteries. *Energy Environ. Sci.* **2020**, *13* (12), 4583–4608. https://doi.org/10.1039/D0EE01638A.

(60) Touja, J.; Gabaudan, V.; Farina, F.; Cavaliere, S.; Caracciolo, L.; Madec, L.; Martinez, H.; Boulaoued, A.; Wallenstein, J.; Johansson, P.; Stievano, L.; Monconduit, L. Self-Supported Carbon Nanofibers as Negative Electrodes for K-Ion Batteries: Performance and Mechanism. *Electrochimica Acta* **2020**, *362*, 137125. https://doi.org/10.1016/j.electacta.2020.137125.

(61) Zhang, Q.; Mao, J.; Pang, W. K.; Zheng, T.; Sencadas, V.; Chen, Y.; Liu, Y.; Guo, Z. Boosting the Potassium Storage Performance of Alloy-Based Anode Materials via Electrolyte Salt Chemistry. *Adv. Energy Mater.* **2018**, *8* (15), 1703288. https://doi.org/10.1002/aenm.201703288.

(62) Caracciolo, L.; Madec, L.; Gachot, G.; Martinez, H. Impact of the Salt Anion on K Metal Reactivity in EC/DEC Studied Using GC and XPS Analysis. *ACS Appl. Mater. Interfaces* **2021**, *13* (48), 57505–57513. https://doi.org/10.1021/acsami.1c19537.

(63) Hosaka, T.; Matsuyama, T.; Kubota, K.; Yasuno, S.; Komaba, S. Development of KPF_6/KFSA Binary-Salt Solutions for Long-Life and High-Voltage K-Ion Batteries. *ACS Appl. Mater. Interfaces* **2020**, *12* (31), 34873–34881. https://doi.org/10.1021/acsami.0c08002.

(64) Madec, L.; Gabaudan, V.; Gachot, G.; Stievano, L.; Monconduit, L.; Martinez, H. Paving the Way for K-Ion Batteries: Role of Electrolyte Reactivity through the Example of Sb-

Based Electrodes. *ACS Appl. Mater. Interfaces* **2018**, *10* (40), 34116–34122. https://doi.org/10.1021/acsami.8b08902.

(65) Zhang, X.; Xiong, T.; He, B.; Feng, S.; Wang, X.; Wei, L.; Mai, L. Recent Advances and Perspectives in Aqueous Potassium-Ion Batteries. *Energy Environ. Sci.* **2022**, *15* (9), 3750–3774. https://doi.org/10.1039/D2EE01573K.

(66) Larhrib, B.; Larbi, L.; Madec, L. Nonaqueous Potassium-Ion Full-Cells: Mapping the Progress and Identifying Missing Puzzle Pieces. *J. Energy Chem.* **2024**, S2095495624000718. https://doi.org/10.1016/j.jechem.2024.01.033.

(67) Larhrib, B.; Madec, L.; Monconduit, L.; Martinez, H. Optimized Electrode Formulation for Enhanced Performance of Graphite in K-Ion Batteries. *Electrochimica Acta* **2022**, *425*, 140747. https://doi.org/10.1016/j.electacta.2022.140747.

(68) Hu, J.; Wu, B.; Chae, S.; Lochala, J.; Bi, Y.; Xiao, J. Achieving Highly Reproducible Results in Graphite-Based Li-Ion Full Coin Cells. *Joule* **2021**, *5* (5), 1011–1015. https://doi.org/10.1016/j.joule.2021.03.016.

(69) Li, X.; Li, J.; Ma, L.; Yu, C.; Ji, Z.; Pan, L.; Mai, W. Graphite Anode for Potassium Ion Batteries: Current Status and Perspective. *ENERGY Environ. Mater.* **2022**, *5* (2), 458–469. https://doi.org/10.1002/eem2.12194.

(70) Hwang, J.-Y.; Kim, J.; Yu, T.-Y.; Jung, H.-G.; Kim, J.; Kim, K.-H.; Sun, Y.-K. A New P2-Type Layered Oxide Cathode with Superior Full-Cell Performances for K-Ion Batteries. *J. Mater. Chem. A* **2019**, *7* (37), 21362–21370. https://doi.org/10.1039/C9TA07837A.

(71) Le Pham, P. N.; Gabaudan, V.; Boulaoued, A.; Åvall, G.; Salles, F.; Johansson, P.; Monconduit, L.; Stievano, L. Potassium-Ion Batteries Using KFSI/DME Electrolytes: Implications of Cation Solvation on the K+-Graphite (Co-)Intercalation Mechanism. *Energy Storage Mater.* **2022**, *45*, 291–300. https://doi.org/10.1016/j.ensm.2021.11.046.